

<b>Title</b>	1
<b>Genome-wide association study in Collaborative Cross mice reveals a role for <i>Rhbdf2</i> in skeletal homeostasis</b>	2
<b>Short title</b>	4
<b>GWAS in mice reveals a new skeletal role for <i>Rhbdf2</i></b>	5
<b>Authors</b>	6
<i>Roei Levy</i> <sup>1,2</sup> , <i>Clemence Levet</i> <sup>3</sup> , <i>Keren Cohen</i> <sup>1</sup> , <i>Matthew Freeman</i> <sup>3</sup> , <i>Richard Mott</i> <sup>4</sup> , <i>Fuad Iraqi</i> <sup>5</sup> , <i>Yankel Gabet</i> <sup>1</sup>	7
<b>Affiliations</b>	9
<sup>1</sup> Department of Anatomy and Anthropology, <sup>2</sup> Department of Human Molecular Genetics and Biochemistry, and <sup>5</sup> Department of Clinical Microbiology and Immunology, Sackler Faculty of Medicine, Tel Aviv University, Tel Aviv 69978, Israel. <sup>3</sup> Dunn School of Pathology, South Parks Road, Oxford OX1 3RE, UK. <sup>4</sup> UCL Genetics Institute, University College London, Gower St., London, WC1E 6BT, UK.	10 11 12 13 14
<b>Keywords</b> Bone; Collaborative Cross; <i>Rhbdf2</i> ; GWAS; <i>iRhom2</i> ; cancellous bone; bone mass; causal genes; femur; RIL	15 16

**Abstract** 17

Osteoporosis, the most common bone disease, is characterized by a low bone mass and 18  
increased risk of fractures. Importantly, individuals with the same bone mineral density 19  
(BMD), as measured on two dimensional (2D) radiographs, have different risks for 20  
fracture, suggesting that microstructural architecture is an important determinant of 21  
skeletal strength. Here we took advantage of the rich phenotypic and genetic diversity 22  
of the Collaborative Cross (CC) mice. Using microcomputed tomography, we 23  
examined key structural parameters in the femoral cortical and trabecular compartments 24  
of male and female mice from 34 CC lines. These traits included the trabecular bone 25  
volume fraction, number, thickness, connectivity, and spacing, as well as structural 26  
morphometric index. In the mid-diaphyseal cortex, we recorded cortical thickness and 27  
volumetric BMD. 28

The broad-sense heritability of these traits ranged between 50 to 60%. We 29  
conducted a genome-wide association study to unravel 5 quantitative trait loci (QTL) 30  
significantly associated with 6 of the traits. We refined each locus by combining 31  
information obtained from the known ancestry of the mice and RNA-Seq data from 32  
publicly available sources, to shortlist potential candidate genes. We found strong 33  
evidence for new candidate genes, including *Rhbd2*, which association to trabecular 34  
bone volume fraction and number was strongly suggested by our analyses. We then 35  
examined knockout mice, and validated the causal action of *Rhbd2* on bone mass 36  
accrual and microarchitecture. 37

Our approach revealed new genome-wide QTLs and a series of genes that have 38  
never been associated with bone microarchitecture. This study demonstrates for the first 39  
time the skeletal role of *Rhbd2* on the physiological remodeling of both the cortical 40

and trabecular bone. This newly assigned function for *Rhbd2* can prove useful in 41  
deciphering the predisposing factors of osteoporosis and propose new investigative 42  
avenues toward targeted therapeutic solutions. 43

**Author summary** 44

In this study, we used the novel mouse reference population, the Collaborative Cross (CC), to identify new causal genes in the regulation of bone microarchitecture, a critical determinant of bone strength. This approach provides a clear advantage in terms of resolution and dimensionality of the morphometric features (versus humans) and rich allelic diversity (versus classical mouse populations), over current practices of bone-related genome-wide association studies. 45  
46  
47  
48  
49  
50

Our genome-wide study revealed 5 loci significantly associated with microstructural traits in the cortical and trabecular bone. We found strong evidence for new candidate genes, in particular, *Rhbd2*. We then validated the specific role of *Rhbd2* on bone mass accrual and microarchitecture using knockout mice. Importantly, this study is the first demonstration of a physiological role for *Rhbd2*. 51  
52  
53  
54  
55

56

**Introduction** 57

Osteoporosis is the most common bone disease in humans, affecting nearly half the US and European population over the age of 50 years. With the globally increasing life expectancy, osteoporosis and related bone fractures are becoming a pandemic health and economic concern. By 2050, the world-wide incidence of hip fractures is expected to increase by 2.5 to 6 fold [1,2]. Importantly, the mortality rate in the 12 months following bone fracture is as high as 20% [3]. Risk of fracture is determined largely by bone density and quality/strength, which are the end result of peak values achieved at skeletal maturity and subsequent age and menopause-related bone loss. Genetic factors have a major role in determining the wide range in the so-called "normal" peak bone 58  
59  
60  
61  
62  
63  
64  
65  
66

mass. Measures of bone status are inherently complex traits, as opposed to Mendelian 67  
traits; i.e. they are controlled by the cumulative effect and interactions of numerous 68  
genetic loci and environmental factors. 69

Genome-wide association studies (GWAS), including a large meta-analysis, 70  
have identified more than 50 loci associated with bone mineral density (BMD) [4–10]. 71  
However, many other genes that were experimentally associated with bone mass were 72  
not confirmed by GWAS in human cohorts [11–13]. This suggests that the BMD 73  
phenotype does not capture the structural complexity of the bone; there may be other 74  
relevant bone phenotypes not yet studied in human GWAS [12], which hitherto have 75  
generally relied on areal bone mineral density (aBMD) as the sole bone feature. aBMD 76  
measured by dual energy x-ray absorptiometry (DXA) is a two-dimensional projection 77  
that cannot measure bone size, individual bone compartments' shape (whether 78  
trabecular or cortical) or underlying microstructure, and thus likely conceals important 79  
features which are assumed to be controlled by unique genetic determinants. Indeed, 80  
there is a growing body of evidence that argues for distinct genetic influences of the 81  
cortical and trabecular bone and thus they should be accordingly distinguished [8,9]. A 82  
recent GWAS in the Collaborative Cross (CC) mice based on DXA failed to find any 83  
heritability of BMD [14], whereas another report based on the same mouse panel 84  
showed highly significant heritability levels in most of the cortical and trabecular 85  
microstructural parameters measured by micro-computed tomography ( $\mu$ CT) [15] 86

Traditional peripheral quantitative CT (pQCT) has the capacity to distinguish 87  
between the cortical and trabecular bone compartments, but it lacks the required 88  
resolution to detect microstructural differences. A recent report based on high 89  
resolution pQCT (HR-pQCT) data in humans, identified two novel bone-related loci, 90

thus far undetected by DXA and pQCT-based GWAS [9]. Another [16], found strong 91  
genetic correlations between 1047 adult participants of the Framingham heart study, 92  
therefore indicating that the heritability of bone microstructure constitutes a phenotypic 93  
layer which is at least partially independent of DXA-derived BMD. Like HR-pQCT 94  
studies in humans, understanding the genetic regulation of bone microstructural 95  
parameters using  $\mu$ CT in small animals is likely to identify genetic factors distinct from 96  
those previously identified for DXA-derived traits. 97

The CC mouse panel is designed to provide high resolution analysis of complex 98  
traits, with particular emphasis on traits relevant to human health [17,18]. This unique 99  
resource currently consists of a growing number of recombinant inbred lines (RIL) 100  
generated from full reciprocal breeding of eight divergent strains of mice [19]. In 101  
contrast to commonly used laboratory mouse strains, the ancestry of the CC lines 102  
includes wild-derived inbred strains that encompass genetic variations accumulated 103  
over ~1 million years [20]; more than 50 million single nucleotide polymorphisms 104  
segregate in founders of the CC. The high genetic diversity means that QTLs can be 105  
mapped using this panel that would have been invisible in a population that involved 106  
only classical strains [21,22]. 107

This claim is substantiated in a recent study that identified a genome-wide 108  
significant association between *Oxt* (oxytocin) and *Avp* (vasopressin) and skeletal 109  
microarchitecture in CC mice [15]. Here, our GWAS in the CC mouse panel identified 110  
a novel gene, *Rhbd2*, associated with bone traits and using a specific knockout model 111  
we validated its role in the regulation of cortical and trabecular bone structure. This 112  
exemplifies the effectiveness and relative ease by which a GWAS with a small CC 113

population can associate a bone-related function to novel genes, and to reveal 114  
overlooked key players in skeletal biology. 115

## Results 116

### CC lines widely differ in bone microarchitecture traits 117

We examined the variation in femoral cortical and trabecular microstructure between 118  
34 unique CC lines totaling in 174 mice (71 females and 103 males, with an average of 119  
4.25 mice per line). In the trabecular bone compartment we measured bone volume 120  
fraction (BV/TV), trabecular number (Tb.N), thickness (Tb.Th), connectivity 121  
(Conn.D), and spacing (or separation; Tb.Sp), as well as structural morphometric index 122  
(SMI) of the trabecular framework. In the mid-diaphyseal cortex, we recorded cortical 123  
thickness (Ct.Th) and volumetric bone mineral density (vBMD). These traits were 124  
approximately normally distributed; BV/TV ranged from 0.017 to 0.26 (i.e. 1.7% to 125  
26%; mean = 10.2%); Tb.N from 0.52 to 6.11 mm<sup>-1</sup> (mean = 2.7 mm<sup>-1</sup>); Tb.Th from 31 126  
to 69 μm (mean = 47 μm); Conn.D from 10.9 to 268.3 mm<sup>-3</sup> (mean = 104.2 mm<sup>-3</sup>); SMI 127  
from 0.6 to 3.3 (mean = 2.3); Tb.Sp from 0.16 to 0.7 mm (mean = 0.33 mm); Ct.Th 128  
from 0.14 to 0.29 mm (mean = 0.2 mm); and vBMD from 402.5 to 809.2 mgHA/cm<sup>3</sup> 129  
(mean = 581.1 mgHA/cm<sup>3</sup>). μCT images taken from two mice with distinct cortical 130  
(Fig. 1A) and trabecular (Fig. 1B) characteristics demonstrate the great variation in 131  
bone traits due solely to the genetic background. Color-codes on the graphs in Fig. 2 132  
indicate Duncan's least significance range (LSR), which dictates whether the mean 133  
value of a line, or a group of lines, for a given trait differs to a degree of at least *P*-value 134  
< 0.001 from any other group. LSR allows for a visual representation of the 135  
heterogeneity amongst the lines. 136

With 11 distinct groups, vBMD (Fig. 2B) is the most heterogeneous trait, while 137  
SMI and Conn.D are the least, with only 3 significantly distinct groups (Fig. 2A). 138  
Notably, the heterogeneity of females is greater than that of males for cortical traits but 139  
milder for trabecular traits (Figs. S1A1, 2 for males and S1B1, 2 for females). 140

141

To examine the inter-dependency between the traits, we assessed the correlation 142  
between all the measured parameters, in a pairwise fashion using Pearson's correlation 143  
test. The strongest correlation was between BV/TV and Tb.N (Pearson's  $r = 0.94$ ), in 144  
line with our previous findings [15], while the weakest was between Tb.N and vBMD 145  
( $r < 0.01$ ). There was also a moderately high correlation between Ct.Th and Tb.Th ( $r =$  146  
0.61; and see Table S1). The correlation between sexes for each trait (Table 1) ranged 147  
from  $r = 0.75$  (Tb.Sp) to  $r = 0.20$  (Ct.Th). Body weight (range = 17.4 - 35.0 gr) did not 148  
significantly correlate with any of the traits ( $r = 0.01$  for Conn.D to  $r = 0.19$  for Ct.Th). 149  
After separating males from females the correlation slightly increased, yet remained 150  
low. Weak correlation was found between weight and Tb.N, SMI, and Ct.Th for 151  
females (Pearson's  $r = -0.20, 0.23,$  and  $0.25$  respectively), and between weight and 152  
Tb.Th and Tb.Sp (Pearson's  $r = 0.25$  and  $-0.25$ ) for males. 153

154

155

156

157

158



**Table 1 Heritability, sex correlations, and covariate interactions for trabecular and cortical traits**

<b>Trait</b>	<b>H<sup>2</sup></b>	<b>logP</b>	<b>H<sup>2</sup>n</b>	<b>Sex Cor.</b>	<b>Interactions %</b>
BV/TV	0.61	12.43	0.87	0.6695754	-
Tb.N	0.63	13.76	0.88	0.7628464	-
Tb.Th	0.54	9.08	0.83	0.7039887	34.70
Conn.D	0.56	9.90	0.84	0.5188039	-
SMI	0.55	9.43	0.84	0.2984166	26.02
Tb.Sp	0.63	13.45	0.88	0.754563	-
vBMD	0.62	12.15	0.87	0.6268818	53.92
Ct.Th	0.51	7.63	0.82	0.2055684	41.07

H<sup>2</sup> is the broad-sense heritability (which includes epistatic and environmental influences); logP is the negative 10-base logarithm of the P-value; H<sup>2</sup>n is the line-mean heritability; Sex Cor. is the sex correlation of each trait; and interactions % refers to the relative contribution of the cumulative covariate-interactions, which include sex, age, batch, month, season, year, and experimenter (see table S2).

159

160

161

162

163

164

165

166

167

Table 2 Positions of QTLs associated with trabecular and cortical traits											
QTL	Trait	Chr	logP	99th % thresh	H <sup>2</sup> <sub>r</sub>	Simulation					
						50% CI (Mb)		90% CI (Mb)		95% CI (Mb)	
						Position	Width	Position	Width	Position	Width
<i>Trl7</i>	BV/TV	11	7.60	4.90	0.69	116.6-116.7	0.12	113.6-118.1	4.50	112.1-118.3	6.40
<i>Trl7</i>	Tb.N	11	6.80	4.84	0.71	116.6-116.87	0.29	114.2-118.35	4.15	112.41-118.68	6.27
<i>Trl8</i>	Tb.Th	4	8.00	4.50	0.61	117.2-117.58	0.32	113.05-125.54	12.49	110.87-126.52	15.65
<i>Trl9</i>	Tb.Sp	5	9.40	6.01	0.78	105.78-106.14	0.35	101.6-109.11	7.54	99.8-110.39	10.62
<i>Crll</i>	Ct.Th	4	8.20	4.80	0.80	9.29-9.72	0.43	4.0-11.7	7.70	3.4-11.8	8.49
<i>Cr12</i>	vBMD	3	9.80	4.93	0.86	97.2-97.4	0.20	94.4-103.1	8.50	93.22-104.3	10.80

Chr = chromosome; logP = negative 10-base logarithm of P value; Sig = genome-wide significance level; 99th % threshold logP = threshold used to define cut-off for QTL peaks (Fig. 4); H<sup>2</sup><sub>r</sub> = regional heritability (the proportion to which the locus explains the phenotypic variability). Positions and widths of the simulation-based 50, 90, and 95% CIs are given.

While in most lines the traits' correlations were predictive of a given line's rank, 170  
in others a less expected pattern was observed; e.g., IL-1513 displayed unusually 171  
extreme phenotypes for all trabecular traits and was at the higher end for BV/TV, Tb.N, 172  
Tb.Th, and Conn.D and at the lower end for SMI and Tb.Sp, but IL-188 was more 173  
discordant between these same traits (Fig. 2 and Table S3), illustrating unexpected co- 174  
variation of the traits in the CC. 175

### Heritability and confounder-control 176

We quantitated the effects of the covariates sex, age, batch, month, season, year, and 177  
experimenter on each trait. Age ranged from 9 (n=6) to 13 (n=9) weeks and the mice 178

were dissected in 20 batches over a three-year course across 8 months during winter, 179  
spring and summer, by two experimenters. Whereas age alone had no effect on any 180  
trait, sex affected only Ct.Th; batch affected Tb.Th, vBMD, and Ct.Th; month affected 181  
Tb.Sp, vBMD, and Ct.Th; season and year affected vBMD and Ct.Th; and Tb.Th and 182  
Ct.Th were affected by experimenter. The cumulative effect of the covariates' pairwise 183  
interactions was noted for Tb.Th, SMI, vBMD, and Ct.Th. (Table S2). 184

We then estimated the broad-sense heritability ( $H^2$ ) of each trait among the CC 185  
lines, which includes additive and non-additive epistatic effects and gene-environment 186  
interactions. The greatest  $H^2$  is seen for Tb.N (0.63,  $\log P = 13.76$ ; where  $\log P$  stands 187  
for the negative 10-base logarithm of the P value and tests the null hypothesis that the 188  
heritability is zero), and the smallest for Ct.Th (0.51,  $\log P = 7.63$ ). 189

We calculated the heritability for the mean values in each line to get a better 190  
representation of the percentage of genetic contribution to the phenotypic heterogeneity 191  
by incorporating  $H^2$  and the average number of lines [23]. This defines  $H^2_n$ , which is 192  
directly proportional to  $H^2$  (Methods; Table 1) and ranges between 82 (Ct.Th) and 88% 193  
(Tb.N and Tb.Sp). 194

Overall the cortical traits seemed more prone to covariate variation; they were 195  
particularly sensitive to sex, batch, and season. This stands in contrast to our previous 196  
results [15] where BV/TV, Tb.N, and Conn.D displayed a profound sex effect, although 197  
there cortical traits were not measured. This means there is a deeper, complex layer of 198  
sex effect dependent upon cooperative environmental and genetical factors which 199  
requires further work to fully comprehend. 200

**Association analysis for microarchitectural traits highlights 5 QTLs** 201

We first measured statistical association between each trait and the founder haplotype 202  
at each locus in the genome. Association analyses of the cortical and trabecular traits to 203  
the haplotypes segregating in the CC (as defined by the ~70 K MegaMuga SNPs) 204  
yielded 5 distinct QTLs. For BV/TV and Tb.N we recognized a marked peak at a locus 205  
of length ~0.45 Mb between 116.5 and 116.9 Mb on chromosome 11, with peak logP 206  
values of 7.6 and 6.8, which extended above the 99<sup>th</sup> percentile permutation-threshold 207  
by 2.7 and 1.94 logP units, respectively. In Tb.Th, Tb.Sp, Ct.Th, and vBMD we 208  
identified different QTLs on chromosomes 4, 5, 4 and 3, with logPs of 8.0, 9.4, 8.2, and 209  
9.8, respectively, above threshold (Fig. 3 and Table 2). To account for false positive 210  
results, we kept the false discovery rate (FDR) at 1% for each scan, by employing the 211  
Benjamini–Hochberg multiple testing procedure on the logPs of the haplotype 212  
associations to the traits. Conn.D and SMI lacked significant peaks above the stringent 213  
permuted threshold and thus were not further analyzed (Fig. S2), but Conn.D 214  
displayed a borderline peak in a region that matches the peak identified for BV/TV and 215  
Tb.N. The 5 QTLs we describe are hereafter referred to as *Trl* (trabecular related locus) 216  
7-9, and *Cr1* (cortical related locus) 1-2 (respectively for BV/TV and Tb.N, Tb.Th, 217  
Tb.Sp, Ct.Th, and vBMD, and in keeping with our previous report [15] that introduced 218  
*Trl* 1-6). The 95% widths of the confidence intervals ranged from 6.4 to 15.6 Mb for 219  
the *Trls*, and were between 8.5-10.8 Mb for the *Cr1s* (Table 2 and Fig. S3). 220

We measured the contribution of each CC founder to the QTLs, relative to the 221  
wild-derived strain WSB/EiJ (Fig. 4). *Trl7* is mostly affected by the classic laboratory 222  
strains 129S1/SvImJ, NOD/LtJ, and NZO/HiLtJ; notably, the other traits were more 223  
strongly driven by the following wild strains: *Trl8* and *Cr12* by PWK/PhJ; *Trl9* by 224  
WSB/EiJ; and *Cr11* by CAST/Ei. 225

For *Trl7*, at the SNP most adjacent to the QTL peak UNC20471277, we found 226  
that the majority of lines with a TT allelic variant (where T refers to the nucleic acid 227  
Thymine) mostly congregate at the higher end of the BV/TV and Tb.N values (Mean 228  
BV/TV = 17%); lines with a CC variant (where C refers to the nucleic acid Cytosine) 229  
are at the lower end (mean BV/TV = 10%); and those with a CT variant are at the 230  
intermediate range (Fig. 5). Largely, the more the trait examined is distantly correlated 231  
with BV/TV, the less differentiated the CC and TT variants are, at the SNP 232  
UNC20471277. This is accentuated in vBMD where there is a weak correlation with 233  
BV/TV (Table S1) and leveled CC and TT groups ( $P$  value = 0.8 Welch's two sample 234  
t-test). 235

### **Candidate genes identified by merge analysis and RNA-seq** 237

To identify the gene most likely driving the skeletal trait, we next performed a merge 238  
analysis and RNA-seq analysis and used a scoring system to rank the potential 239  
candidates. 240

Merge analysis uses the catalogue of variants segregating in the eight CC 241  
founders to impute the genotype dosage of each SNP in each CC line, based on the 242  
haplotype reconstruction used for haplotype association [24]. Candidate causal 243  
variants, if they exist, would be expected to be more significant (have higher logP 244  
values) than the haplotype-based test in the flanking region. We found that *Trl7* had the 245  
highest density of polymorphisms (grey and crimson dots in Fig. 6) with merge-logP 246  
values above the haplotype logPs (continuous black line in Fig. 6), while *Trl8* and *Cr12* 247  
had very few. The merge logP values of the two latter loci congregated more upstream, 248

in accordance with the left-skewness of their respective CI simulations (Fig. 6; Fig. S3). 249  
By calculating the relative density of merge logP values which are considerably higher 250  
than the haplotype merge logPs -and above the 99<sup>th</sup> percentile threshold for each scan - 251  
at intervals defined by each gene within the QTLs (in meaningful regions; usually 252  
between the 50<sup>th</sup> and 90<sup>th</sup> CI percentile) we could rank the genes according to their 253  
merge analysis results (Table S4). For example, while the proportion of merge analysis 254  
SNPs for BV/TV and Tb.N with logPs greater than that of the haplotype scan is 1.4% 255  
at the genome-wide scale (as well as at the region spanning the 95% CI, between ~112 256  
– 118 Mb), it is 9.4% and ranked 5/36 (for BV/TV) or 14.07% and ranked 3/36 (for 257  
Tb.N) at the region in which the gene *Rhbd2* is situated (~116.5 – 116.6 Mb) (See 258  
Table S4 and further discussion below). 259

To strengthen the criteria that classifies potential putative candidate gene as true 260  
positives, we analyzed RNA-seq datasets of osteoclasts (Fig. S4) and osteocytes (Fig. 261  
S5) made publicly available by Kim *et al.* [25] (Gene Expression Omnibus accession 262  
number GSE72846) and St John *et al.* [26] (Gene Expression Omnibus accession 263  
number GSE54784). We focused on local maximas that span ~0.5 Mb in and around 264  
the peaks suggested by the merge analysis, for each QTL. From the raw count reads we 265  
found that *Trl7* had the strongest gene expression differential; e.g while *Mxra7* in the 266  
osteoclasts was expressed to a negligible degree (Fig. S4A), it had a strong presence in 267  
osteocytes (Fig. S5A), whereas the genes of the other loci had much less prominent 268  
differences. This suggests that genes at *Trl7* are differentially expressed between 269  
osteocytes and osteoclasts more prominently than in the other loci. 270

For each of the genes with the highest merge analysis scores in *Trl7*, we 271  
attributed an *osteoclast* and *osteocyte* RNA-seq ( $S_{\text{RNA-seq1}}$  and  $S_{\text{RNA-seq2}}$ , respectively) 272

score based on the following formula:  $S_{RNA-seq} = 1 - \frac{r}{n}$ ; where  $r$  is the local gene rank 273  
(sorted by the raw read count) and  $n$  is the total number of genes at the locus, where 274  
 $n=10$ , if  $n>10$ . For example, *Ube2o* had an *osteoclast* RNA-seq score of 0.8 (ranked 2<sup>nd</sup> 275  
out of  $n>10$  genes) and *osteocyte* RNA-seq score of 0.8. *Rhbd2* had an *osteoclast* RNA- 276  
seq score of 0.9 (ranked 1<sup>st</sup>) and *osteocyte* RNA-seq score of 0.7. 277

We then summed up the cumulative *MS* (**M**erge and **S**equencing) score for each 278  
gene, defined as  $MS(i) = \ln(M_{strength}(i)) + (S_{RNA-seq1}(i) + S_{RNA-seq2}(i))$ , where  $M_{strength}$ ,  $S_{RNA-$  279  
 $seq1$ , and  $S_{RNA-seq2}$  refer to the merge rank (or strength), osteoclast RNA-seq score, and 280  
osteocyte RNA-seq score of a given gene ( $i$ ), respectively. Our analytical approach and 281  
scoring system enabled us to shortlist the most plausible causal genes at the QTLs. In 282  
*Trl7*, *Ube2o* had an  $MS_{Ube2o} = 2.4 + (0.8 + 0.8) = 4.0$ ; while *Aanat* scored  $MS_{Aanat} = 2.7$  283  
 $+ (0 + 0) = 2.7$ , and *Rhbd2* scored  $MS_{Rhbd2} = 2.6 + (0.9 + 0.7) = 4.2$ . In the other loci, 284  
the highest ranked genes were *Klf17* and *Kdm4a* for *Trl8*; *Barhl2* and *Zfp644* for *Trl9*; 285  
*Asph* and *Gdf6* for *Crl1*; and *Hfe2*, *Acp6*, *Bcl9*, and *Notch2* for *Crl2*. 286

Because BV/TV is a predominant parameter in bone biology, we first focused 287  
on *Trl7*. *Rhbd2* had a merge strength of 14% (the 3<sup>rd</sup> strongest at the QTL and 2<sup>nd</sup> at 288  
the 50% CI), and a local maxima at the RNA-seq of the osteoclasts. It was located near 289  
the haplotype mapping peak, and because it received the highest cumulative *MS* score, 290  
*Rhbd2* was retained for validation. The comprehensive list of the genes under the 50, 291  
90, and 95% CI of the QTL, is supplied in table S4. 292

### **Validation of the skeletal role of *Rhbd2* in knock-out mice** 293

Femora of male mice ( $n=14$ ) null at *Rhbd2* (on a C57Bl/6J background) were collected, 294  
on which we measured the same morphometric traits as above, including BV/TV, Tb.N, 295

Tb.Th, SMI, Tb.SP, Ct.Th, and vBMD. These were compared to their wild-type (WT) 296  
counterparts (n=13), after adjusting for batch, age and weight. 297

Strikingly, we found that *Rhbd2*<sup>-/-</sup> mice had a significant bone phenotype. In 298  
line with our GWAS data, *Rhbd2*<sup>-/-</sup> mice displayed a highly significant increase in 299  
BV/TV and Tb.N (Fig. 7, 8). As expected, *Rhbd2* KO also affected other 300  
microstructural parameters, partly due to the high correlation between the trabecular 301  
traits. After adjusting for confounders, we observed a significant difference between 302  
KO and WT animals in Tb.Sp (P value < 0.001; uncorrected P value = 0.017), SMI (P 303  
value = 0.03; uncorrected P value = 0.156) and Conn.D (P value = 0.008; uncorrected 304  
P value = 0.046). Tb.Th and vBMD were not affected by the knockout. Although the 305  
cortical compartment did not display a haplotype peak at the vicinity of *Trl7* in the CC 306  
animals. However, after adjusting for confounders, we observed a significant difference 307  
in Ct.Th between KO and WT bones (P value = 0.01), suggesting that the role of *Rhbd2* 308  
is not limited to the trabecular compartment (Fig. 7). 309

## Discussion 310

Genetic reference population (GRP) are very efficient for the study of complex traits 311  
and biological systems, because (i) genotyping is only required once (“genotype once, 312  
phenotype many times”, see below), and (ii) replicate individuals with the same 313  
genotype can be generated at will allowing for optimal experimental designs [27]. 314

This article is the second to present the results of an ongoing quest to delineate 315  
the genetic determinants that govern microstructural bone traits [15]. Here we 316  
characterize several key microstructural properties of the mouse femoral bone to assess 317  
the extent to which they are heritable; to what environmental perturbations they are 318



prone; and to identify candidate genes by which they are controlled. Our approach 319  
narrowed down a small number of putative candidate genes for 6 of the 8 examined 320  
phenotypes. Following merge analysis and RNA-seq, we validated our leading 321  
candidate gene, *Rhbd2*, using a knockout model, which confirmed the critical role of 322  
*Rhbd2* on bone mass accrual and homeostasis. 323

While the heritability rates assessed here - determined to be over 60% for all 324  
traits - confirmed our previous findings, the degree to which sex explains the 325  
phenotypic variation was very subtle, and appeared only for the cortical traits; this 326  
discrepancy may be due to the specific cohort composition used in this study (Table 327  
S3), which includes a sex bias due to smaller number of females than males. We found 328  
a total of five QTLs in six traits; BV/TV and Tb.N shared one QTL, and Tb.Th, Tb.Sp, 329  
vBMD, and Ct.Th yielded one each. Importantly, although bone microarchitecture 330  
factors are complex traits, our analyses highlighted no more than two loci for each trait; 331  
it is likely that analyzing a larger number of CC lines would result in the identification 332  
of further loci. 333

Our analyses yielded three QTLs for the trabecular traits and 2 QTLs for the 334  
cortical traits. These are referred to as *Trl7-9*, and *Cr11-2*, respectively. In addition, and 335  
in close proximity, to *Rhbd2* (Rhomboid 5 Homolog 2; elaborated below), *Trl7* 336  
includes *Ube2o* (Ubiquitin Conjugating Enzyme E2 O), which encodes an enzyme that 337  
is an important interactant of SMAD6. Ube2o monoubiquitinates SMAD6, and thereby 338  
facilitates the latter to bind BMP 1 receptors [28]. The signal transduction of BMP 1 is 339  
in turn limited [29,30], and endochondral bone formation, instead of ossification, is 340  
favored. Importantly, 4 week-old SMAD6-overexpressed mice have significantly lower 341  
humeral and vertebral BV/TV ratios than their controls [29]. 342

At *Trl8*, *Klf17*, *Kdm4a*, and *Dmap1* are likely putative candidate genes. Since 343  
*Klf17* (Kruppel-Like Factor 17) is part of a network that includes BMPs [31] it is more 344  
likely than a nearby gene, *St3gal3* (ST3 Beta-Galactoside Alpha-2,3-Sialyltransferase 345  
3), to affect bone traits, although the latter has a greater merge strength. *Kdm4a* (Lysine 346  
Demethylase 4A) encodes a histone demethylase that promotes the differentiation of 347  
embryonal stem cells (ESCs) to an endothelial fate [32]; endothelial cells are implied 348  
in regulation of bone formation [33]. *Dmap1* (DNA Methyltransferase 1 Associated 349  
Protein) which encodes a DNA-methyl transferase known to regulate obesity 350  
complications, and is differentially methylated in women with polycystic ovary 351  
syndrome [34,35] had the highest meaningful merge density, and it might 352  
epigenetically regulate bone formation as well. *Trl9* includes two genes of interest to 353  
bone biology: *Barhl2* and *Zfp644*. By interacting with caspase3, which is essential for 354  
ossification [36], *Barhl2* (BarH Like Homeobox 2) can inhibit  $\beta$ -catenin activation [37], 355  
and regulate the expression of chordin, a BMP signaling-detrimental protein [38]. 356  
*Zfp644* (Zinc Finger Protein 644), which encodes a transcription repressor zinc-finger 357  
protein, is upregulated in eight week-old ovariectomized mice following treatment with 358  
estradiol [39], a treatment associated with reduced bone loss [40]. Further support for 359  
the candidacy of *Barhl2* and *Zfp644* is given by the role of *Barhl2* in the development 360  
of amacrine cells [41,42] and the association of *Zfp644* with myopia [43], a condition 361  
speculated to propagate from amacrine cell signaling [44]; interestingly myopia was 362  
linked to reduced postnatal bone mineral content in humans [45] and decreased 363  
expression of BMP 2 and 5 in guinea pigs [46]. 364

The first of two cortical loci, *Cr11* contains as likely candidates the genes *Asph* 365  
and *Gdf6*. *Asph* (Aspartate Beta-Hydroxylase) encodes a protein that has a role in 366  
regulating calcium homeostasis, which may affect bone metabolism [47]. *Gdf6* (Growth 367

Differentiation Factor 6) is bone morphogenetic protein 13: mice with mutated *Gdf6* 368  
exhibit deformed bone formation in various skeletal sites; it is among the earliest known 369  
markers of limb joint formation [48], expressed in joints of ankle and knee. In *Gdf6* 370  
homozygous mutant mice, bones fuse at the joints early at the segmentation stage [49]. 371  
For *Crl2*, we found *Hfe2*, *Bcl9*, *Notch2*, and *Prkab2* as potential candidate genes. *Hfe2* 372  
(Hemochromatosis Type 2 (Juvenile)) encodes the BMP co-receptor hemojuvelin 373  
which is expressed in skeletal muscles [50] and is responsible for juvenile 374  
hemochromatosis, a condition linked to sex hormones depletion and osteoporosis [51]. 375  
*Bcl9* (B-Cell CLL/Lymphoma 9), the mammalian ortholog of the gene *Legless*, encodes 376  
a protein essential to the Wnt/beta-catenin signaling which is important for bone 377  
metabolism [52], without which the nuclear localization of  $\beta$ -catenin and myocyte 378  
differentiation are compromised [53]. Of note, there are mutual effects between bone 379  
and muscle, and accumulating evidence suggest many genes show pleiotropism with 380  
respect to muscle strength and bone parameters [54]. *Notch2* encodes a member of the 381  
notch protein family, which influence both osteoblasts and osteoclasts [55]; 382  
specifically, *Notch2* is associated with the rare Hajdu-Cheney syndrome, that includes 383  
severe osteoporosis as one of its main symptoms [56,57]. For this gene, we did not find 384  
any significant merge logPs included within its limits. Interestingly, *Sec22b*, an 385  
adjacent gene, had the strongest merge logP marks in this locus but no documented link 386  
to bone biology. The third-strong gene in terms of merge values was *Prkab2* (Protein 387  
Kinase AMP-Activated Non-Catalytic Subunit Beta 2). It encodes an enzyme which is 388  
the regulatory subunit of mitogen-activated protein kinase (AMPK). AMPK widely 389  
affects bone metabolism [58]. 390

*Rhbd2* is not yet supported by peer-reviewed reports as bearing a relation to 391  
bone. Based on its closeness to the *Tlr7* peak (within the 50% CI), its merge strength 392

and RNA-seq in bone cells, we identified *Rhbd2* as a likely causal gene associated with 393  
BV/TV and Tb.N. We therefore analyzed the bone phenotype of *Rhbd2*<sup>-/-</sup> mice, to 394  
validate the role of this gene in the modeling of the femoral cortex and trabeculae. 395  
*Rhbd2* deletion affected all the examined trabecular traits as well as Ct.Th. While the 396  
effects on BV/TV and Tb.N were in line with the haplotype mapping, the *Rhbd2* locus 397  
did not appear in any of the other traits. This however is expected, because the genetic 398  
architecture of the working cohort is such that the assumed contributing variant of 399  
*Rhbd2* is diluted and compensated, resulting in a QTL detected only for the most 400  
affected traits. Noticeably, Tb.Sp differed greatly between the *Rhbd2*<sup>-/-</sup> and control 401  
mice but did not show up at the haplotype mapping; this might be due to (i) the great 402  
diversity of the wild-type mice in Tb.Sp, and/or (ii) the need for complete knockout 403  
rather than a mere SNP to detect significant changes in Tb.Sp, and/or (iii) the SNPs 404  
giving rise to *Tr17* are functioning variants, with differential behavior affecting only 405  
BV/TV and Tb.N. A similar interpretation may be valid for the cortical phenotype of 406  
the *Rhbd2*<sup>-/-</sup> mice. Importantly, the significant QTL peak we found in our GWAS for 407  
BV/TV and Tb.N ended up revealing a gene that has an important skeletal function in 408  
both the trabecular and cortical bone compartments. 409

*Rhbd2* encodes the iRhom2 protein, a polytopic membrane protein that is a 410  
catalytically inactive member of the rhomboid intramembrane serine proteases 411  
superfamily [59]. iRhom2 is necessary in macrophages for the maturation and release 412  
of the inflammatory cytokine tumor necrosis factor  $\alpha$  (TNF $\alpha$ ): it acts in the trafficking 413  
of TACE, the protease that releases active TNF $\alpha$  from its membrane-tethered precursor 414  
[60,61]. iRhom2 is also implicated in EGF-family growth factor signaling [62–64]. 415  
With a recent report of its role in trafficking of another protein, STING, it appears that 416  
iRhom2 may have a wider role in regulating membrane trafficking [65]. iRhom2 was 417

also implicated in the regulation of CSF1R (macrophage stimulating factor 1 receptor), 418  
a critical regulator of osteoclasts differentiation and survival [61,66–68]. *In vivo*, 419  
*Rhbd2* has been implicated in esophageal cancer, wound healing, bone marrow 420  
repopulation by monocytic cells, and inflammatory arthritis [63,69–71]. 421

Further work will be needed to identify the mechanism by which iRhom2 422  
controls bone homeostasis; a possible direction could involve a positive feedback loop 423  
that leads to differentiation of macrophages to osteoclasts. Indeed, iRhom2 stimulates 424  
the secretion of TNF $\alpha$  by macrophages [68,72]; hyperactivates EGFR [73,74]; and 425  
regulates CSF1R [75,76]. Although *Rhbd2* is expressed in both the osteocyte and 426  
osteoclast lineages, one cannot rule out the possibility that this gene regulates bone 427  
remodeling by virtue of its expression in non-skeletal cells. 428

In summary, our analyses disclose several putative genes, several of which are 429  
newly linked to a role in bone biology. A confirmation of one such gene, *Rhbd2*, 430  
provides the first conclusive evidence for its effects on bone microstructure. 431  
Importantly, this study is the first demonstration of a physiological role of *Rhbd2*. This 432  
finding prompts future investigations to elucidate the exact mechanism of action of 433  
*Rhbd2* and its contribution to osteoporosis in humans. 434

## **Materials and Methods** 435

### Mice 436

Mice aged 10 to 13 weeks (male  $n = 103$ ; female  $n = 71$ ), from 34 different CC lines 437  
(average of 5 mice per line) were used in this study. The mice were at inbreeding 438  
generations of 11 to 37, which correspond to 80-99.9% genetic homozygosity, 439  
respectively. The mice were bred and maintained at the small animal facility of the 440

Sackler Faculty of Medicine, Tel Aviv University (TAU), Israel. They were housed on 441  
hardwood chip bedding in open-top cages, with food and distilled water available *ad* 442  
*libitum*, in an identical controlled environment (temperature =  $25 \pm 2^\circ\text{C}$ ; 60%  $\leq$  443  
humidity  $\leq$  85%) and a 12-hour light/dark cycle. All experiments protocols were 444  
approved by the Institutional Animal Care and Use Committee (IACUC M-13-014) at 445  
TAU, which follows the NIH/USA animal care and use protocols. The *Rhbd2* knock 446  
out mice and their WT counterparts were bred and maintained at the University of 447  
Oxford as approved by license PPL80/2584 of the UK Home Office. 448

#### Specimen collection 449

Mice were intraperitoneally euthanized with cervical dislocation performed 450  
approximately one minute after breathing stops owing to 5% Isoflurane inhalation. The 451  
*Rhbd2* knock out mice and their WT counterparts were euthanized by inhalation of a 452  
rising concentration of carbon dioxide followed by dislocation of the neck. Left femora 453  
were harvested and fixed for 24 hours in 4% paraformaldehyde solution, and then stored 454  
in 70% ethanol. 455

#### $\mu$ CT evaluation 456

Whole left femora from each mouse were examined as described previously [77] by a 457  
 $\mu$ CT system ( $\mu$ CT 50, Scanco Medical AG, Switzerland). Briefly, scans were 458  
performed at a 10- $\mu\text{m}$  resolution in all three spatial dimensions. The mineralized tissues 459  
were differentially segmented by a global thresholding procedure [78]. All 460  
morphometric parameters were determined by a direct 3D approach [79]. Parameters 461  
analyzed were determined in the metaphyseal trabecular bone, which included 462  
trabecular bone volume fraction (BV/TV; %), trabecular thickness (Tb.Th;  $\mu\text{m}$ ), 463  
trabecular number (Tb.N;  $\text{mm}^{-1}$ ), trabecular connectivity density (Conn.D;  $\text{mm}^{-3}$ ), 464

trabecular structure model index (SMI), and trabecular separation (Tb.Sp; mm). Two 465  
additional parameters are characteristics of the mid-shaft diaphysis section, and include 466  
volumetric bone mineral density (vBMD; mgHA/cm<sup>3</sup> [mg Hydroxy-Apatite per cm<sup>3</sup>]) 467  
and cortical thickness (Ct.Th; mm). All parameters were generated and termed 468  
according to the Guidelines for assessment of bone microstructure in rodents using 469  
micro-computed tomography [80]. 470

### Genotyping 471

A representative male mouse from each line was initially genotyped with a high mouse 472  
diversity array (MDA), which consists of 620,000 SNPs (Durrant et al., 2011). After 473  
about two intervals of 4 generations of inbreeding, all the CC lines were re-genotyped 474  
by mouse universal genotype array (MUGA, 7,500 markers) and finally with the 475  
MegaMuga (77,800 markers) SNP array to confirm their genotype status [19]. The 476  
founder-based mosaic of each CC line was reconstructed using a hidden Markov model 477  
(HMM) in which the hidden states are the founder haplotypes and the observed states 478  
are the CC lines, to produce a probability matrix of descent from each founder. This 479  
matrix was then pruned to about 11,000 SNPs by averaging across a window of 20 480  
consecutive markers for faster analyses and reduction of genotyping errors [81]. 481

### Statistical analyses and data acquisition 482

All statistical analyses were performed with the statistical software R (R core 483  
development team 2009), including the package happy.hbrem [82]. 484

*Heritability and covariate effects.* Broad-sense heritability ( $H^2$ ) was obtained for each 485  
trait by fitting the trait (the independent variable) to the CC line label in a linear 486  
regression model that incorporates relevant covariates (sex, age, batch, month, season, 487

year, and experimenter). ANOVA test was used to compare a null model (in which all 488  
dependent variables are set to 0) with linear models that fit the covariates and the CC 489  
line labels to the examined trait. Practically, the difference between the residual sum of 490  
squares ( $RSS; \sum_1^n (\mu_i - \hat{\mu}_i)^2$ ) of the covariates model and that of the CC-line labels 491  
can be seen as the net genetic contribution to the trait. Thus, this difference divided by 492  
that of the covariate model gives an estimation of the heritability. Each covariate was 493  
calculated separately, by dividing the RSS difference between the null and full model 494  
with that of the null model. Let  $F_0$  be the model that fits the trait to the covariates;  $F_1$  495  
the model that fits the trait to the covariates and the CC line label; and  $F_{00}$  the null 496  
model. Then, employing ANOVA, heritability is: 497

$$H^2 = (RSS(F_0) - RSS(F_1)) / RSS(F_{00}). \quad 498$$

Similarly, the effects for each covariate were computed separately, by fitting each in 499  
 $F_0$ . The covariate effect is thus: 500

$$(RSS(F_{00}) - RSS(F_1)) / RSS(F_{00}). \quad 501$$

$H^2_n$  was derived from  $H^2$  according to Atamni *et al.* [23]. 502

*Haplotype mapping.* Each trait was fitted in a multiple linear regression model to the 503  
probability matrix of descent from each founder, including sex and age as covariates. 504

The expected trait value from two ancestors, termed the genetic fit, is: 505

$$\mu_i = \mu + \sum_{s,t} F_{Li}(s,t)(\beta_s + \beta_t) = \mu + \sum_s \sum_t F_{Li}(s,t)\beta_s \quad 506$$

where  $\mu$  is a normally distributed trait mean, with sex and age incorporated;  $F_{Li}(s,t)$  is 507  
the probability of descent from founders  $s$  and  $t$ ; and  $\beta_s + \beta_t$  is the additive effect of 508  
founders  $s$  and  $t$ . Because  $\sum_s \sum_t F_{Li}(s,t) = 2$  for a diploid organism, the maximum 509



likelihood estimates  $\hat{\beta}_s$  are not independent. Thus, they are expressed here as 510  
differences from the WSB/EiJ founder effect, so that  $\hat{\beta}_{WSB} = 0$ . Number of members 511  
per line was weighted and integrated in the linear model. ANOVA was then used to 512  
compare this model with a null model where the founder effects are all set to 0; the 513  
resulting  $F$ -statistic yielded the significance of the genetic model vs. the null model and 514  
the negative 10-base logarithms of the P values ( $\log P$ ) were recorded. 515

Permutations of the CC lines between the phenotypes were used to set 516  
significance thresholds levels. Founder effects are the estimates derived from the 517  
multiple linear regression fit above. 518

Regional heritability ( $H_r^2$ ) was hereafter computed by ANOVA as in the broad- 519  
sense heritability computation, except that here null linear regression fit was compared 520  
with a genetic linear regression fit with the probability matrix of the founder descent at 521  
the peak QTL as the explanatory variable. 522

False discovery rate (FDR) was calculated using the `p.adjust` function in R, with 523  
the method "BH" (Benjamini-Hochberg [83]). 524

*Confidence intervals.* Confidence intervals (CIs) were obtained both by simulations and 525  
by the quick method of Li, 2011 [84]. In the simulations, we resampled the residuals of 526  
the original linear regression fit at the peak of each QTL and rescanned 100 intervals 527  
within 7-10 Mb of the original loci to find the highest  $\log P$ . Accordingly, following 528  
Durrant *et al.* [22], 1000 QTLs were simulated: if  $\hat{t}_i$  is a random permutation of the 529  
residuals of fitted genetic model at the QTL peak, and  $K$  is a marker interval in a 530  
neighborhood of 3.5 to 5 Mb of the QTL peak  $L$ , a set of values for each trait,  $Z_{iK}$  is 531  
provided by: 532

$$Z_{iK} = \hat{t}_i \exp(\hat{\mu} + \sum_s X_{Kis} \hat{\beta}_s). \quad 533$$

*Merge analysis.* In the merge analysis the eight founder strains are partitioned and merged according to the strain distribution pattern (SDP) of the alleles at the quantitative trait nucleotides (QTN) within a given QTL (formerly obtained by the initial mapping). If we denote the polymorphism as  $p$ , then  $X_p = 1$  if  $s$  has allele  $a$  at  $p$ , and  $X_p = 0$  otherwise [24]. Then, at  $p$ , the probability of  $i$  to inherit alleles  $a$  and  $b$  from  $s$  and  $t$ , respectively, within  $L$  is

$$G_{pi}(a, b) = \sum_{s,t} X_p(a, s) X_p(b, t) F_{Li}(s, t). \quad 540$$

This merges the founder strains by  $p$ . The expected trait value in the merged strains can now be inferred by

$$\sum_{a,b} G_{pi}(a, b) (\beta_a + \beta_b). \quad 543$$

Because this is a sub-model of the QTL model, it is expected to yield higher logP values due to a reduction in the degrees of freedom. Significance was obtained by comparing the merge model with the QTL model. Individual genes were extracted from the Sanger mouse SNP repository ([http://www.sanger.ac.uk/sanger/Mouse\\_SnpViewer](http://www.sanger.ac.uk/sanger/Mouse_SnpViewer)).

*Merge strength.* We ranked the list of genes under each QTL according to the density of merge logPs associated with them: only genes that had merge logPs above the haplotype mapping reading, and above the threshold, plus logP=1 were included. We then computed the relative density according to the density of a given gene's merge logPs versus the locus' merge logP density. Let  $g$  be the region encompassed by a gene;  $l$  the region encompassed by a QTL; and  $mp$  the merge logP values above the haplotype

P values plus 1. Then  $g_i(mp) = 1$  if at SNP  $i$  there exists a  $mp$  and 0 otherwise. 554

Similarly  $l_j(mp) = 1$  if at SNP  $j$  there exists a  $mp$  and 0 otherwise. The merge strength 555

( $M_{strength}$ ) is therefore: 556

$$M_{strength} [\%] = 100 * \frac{\sum_i g_i(mp)}{\sum_j l_j(mp)} \%.$$
 557

*RNA-seq data.* RNA-seq data from osteoclasts and osteocytes was obtained from gene 558

expression omnibus (GEO) database (accession numbers GSE72846 and GSE54784) 559

and mapped to the *mus musculus* assembly mm10 using tophat v. 2 [85]. Read counts 560

were then casted on the loci of interest using the R (R Core Team 2015) package 561

GenomicAlignments and raw read counts were taken. For the osteocytes, the data of 562

basal level day 3 was averaged. 563

*MS score.* Based on the merge analysis and RNA-seq data we ranked each gene 564

according to the score in each category:  $MS(i) = \ln(M_{strength}(i)) + (S_{RNA-seq1}(i) + S_{RNA-}$  565

$seq2(i))$ , where  $MS$ ,  $M_{strength}$ ,  $S_{RNA-seq1}$ , and  $S_{RNA-seq2}$  refer to the **merge** and **sequencing** 566

score, merge rank (or strength), osteoclast RNA-seq score, and osteocyte RNA-seq 567

score of a given gene ( $i$ ), respectively.  $S_{RNA-seq1,2}$  scores were generated according to the 568

formula  $S_{RNA-seq} = 1 - \frac{r}{n}$ ; where  $r$  is the local gene rank (sorted by the raw read count) 569

and  $n$  is the total number of genes at the locus, where  $n=10$ , if  $n>10$ . 570

571

572

**Acknowledgments** 573

This study was supported by Tel Aviv University starter funds and by Israel Science 574

Foundation (ISF) grant 1822/12 to YG, by Wellcome Trust grants 085906/Z/08/Z, 575

075491/Z/04, and 090532/Z/09/Z to RM, core funding by Tel-Aviv University to FI, 576  
Wellcome Trust grant 101035/Z/13/Z and the Medical Research Council (programme 577  
number U105178780) to MF, and by a fellowship from the Edmond J. Safra Center for 578  
Bioinformatics at Tel-Aviv University to RL. 579

## References 580

1. Burge R, Dawson-Hughes B, Solomon DH, Wong JB, King A, Tosteson A. 581  
Incidence and economic burden of osteoporosis-related fractures in the United 582  
States, 2005-2025. *J Bone Miner Res.* 2007;22: 465–75. 583  
doi:10.1359/jbmr.061113 584
2. Dhanwal DK, Dennison EM, Harvey NC, Cooper C. Epidemiology of hip 585  
fracture: Worldwide geographic variation. *Indian J Orthop.* 2011;45: 15–22. 586  
doi:10.4103/0019-5413.73656 587
3. Center JR, Nguyen T V, Schneider D, Sambrook PN, Eisman JA. Mortality 588  
after all major types of osteoporotic fracture in men and women: an 589  
observational study. *Lancet (London, England).* 1999;353: 878–82. 590  
doi:10.1016/S0140-6736(98)09075-8 591
4. Mizuguchi T, Furuta I, Watanabe Y, Tsukamoto K, Tomita H, Tsujihata M, et 592  
al. LRP5, low-density-lipoprotein-receptor-related protein 5, is a determinant 593  
for bone mineral density. *J Hum Genet.* 2004;49: 80–6. doi:10.1007/s10038- 594  
003-0111-6 595
5. Richards JB, Rivadeneira F, Inouye M, Pastinen TM, Soranzo N, Wilson SG, et 596  
al. Bone mineral density, osteoporosis, and osteoporotic fractures: a genome- 597  
wide association study. *Lancet.* 2008;371: 1505–12. doi:10.1016/S0140- 598  
6736(08)60599-1 599

6. Styrkarsdottir U, Halldorsson B V, Gretarsdottir S, Gudbjartsson DF, Walters GB, Ingvarsson T, et al. Multiple genetic loci for bone mineral density and fractures. *N Engl J Med.* 2008;358: 2355–65. doi:10.1056/NEJMoa0801197
7. Trikalinos TA, Salanti G, Zintzaras E, Ioannidis JPA. Meta-analysis methods. *Adv Genet.* 2008;60: 311–34. doi:10.1016/S0065-2660(07)00413-0
8. Estrada K, Styrkarsdottir U, Evangelou E, Hsu Y-H, Duncan EL, Ntzani EE, et al. Genome-wide meta-analysis identifies 56 bone mineral density loci and reveals 14 loci associated with risk of fracture. *Nat Genet.* 2012;44: 491–501. doi:10.1038/ng.2249
9. Paternoster L, Lorentzon M, Vandenput L, Karlsson MK, Ljunggren O, Kindmark A, et al. Genome-wide association meta-analysis of cortical bone mineral density unravels allelic heterogeneity at the RANKL locus and potential pleiotropic effects on bone. *PLoS Genet.* 2010;6: e1001217. doi:10.1371/journal.pgen.1001217
10. Paternoster L, Lorentzon M, Lehtimäki T, Eriksson J, Kähönen M, Raitakari O, et al. Genetic determinants of trabecular and cortical volumetric bone mineral densities and bone microstructure. *PLoS Genet.* 2013;9: e1003247. doi:10.1371/journal.pgen.1003247
11. Jovanovich A, Buzková P, Chonchol M, Robbins J, Fink HA, de Boer IH, et al. Fibroblast growth factor 23, bone mineral density, and risk of hip fracture among older adults: the cardiovascular health study. *J Clin Endocrinol Metab.* 2013;98: 3323–31. doi:10.1210/jc.2013-1152
12. Hsu Y-H, Kiel DP. Clinical review: Genome-wide association studies of skeletal phenotypes: what we have learned and where we are headed. *J Clin*

- Endocrinol Metab. 2012;97: E1958-77. doi:10.1210/jc.2012-1890 624
13. Styrkarsdottir U, Thorleifsson G, Sulem P, Gudbjartsson DF, Sigurdsson A, 625  
Jonasdottir A, et al. Nonsense mutation in the LGR4 gene is associated with 626  
several human diseases and other traits. Nature. Nature Publishing Group, a 627  
division of Macmillan Publishers Limited. All Rights Reserved.; 2013;497: 628  
517–20. doi:10.1038/nature12124 629
14. Iraqi F a, Athamni H, Dorman A, Salymah Y, Tomlinson I, Nashif A, et al. 630  
Heritability and coefficient of genetic variation analyses of phenotypic traits 631  
provide strong basis for high-resolution QTL mapping in the Collaborative 632  
Cross mouse genetic reference population. Mamm Genome. 2014;25: 109–19. 633  
doi:10.1007/s00335-014-9503-5 634
15. Levy R, Mott RF, Iraqi FA, Gabet Y. Collaborative cross mice in a genetic 635  
association study reveal new candidate genes for bone microarchitecture. BMC 636  
Genomics. 2015;16: 1013. doi:10.1186/s12864-015-2213-x 637
16. Karasik D, Demissie S, Zhou Y, Lu D, Broe KE, Bouxsein ML, et al. 638  
Heritability and Genetic Correlations for Bone Microarchitecture: The 639  
Framingham Study Families. J Bone Miner Res. 2016; doi:10.1002/jbmr.2915 640
17. Threadgill DW, Hunter KW, Williams RW. Genetic dissection of complex and 641  
quantitative traits: from fantasy to reality via a community effort. Mamm 642  
Genome. 2002;13: 175–8. doi:10.1007/s00335-001-4001-Y 643
18. Churchill G a, Airey DC, Allayee H, Angel JM, Attie AD, Beatty J, et al. The 644  
Collaborative Cross, a community resource for the genetic analysis of complex 645  
traits. Nat Genet. 2004;36: 1133–7. doi:10.1038/ng1104-1133 646
19. Collaborative Cross Consortium. The genome architecture of the Collaborative 647

Cross mouse genetic reference population. *Genetics*. 2012;190: 389–401. 648  
doi:10.1534/genetics.111.132639 649

20. Keane TM, Goodstadt L, Danecek P, White M a, Wong K, Yalcin B, et al. 650  
Mouse genomic variation and its effect on phenotypes and gene regulation. 651  
*Nature*. 2011;477: 289–94. doi:10.1038/nature10413 652

21. Roberts A, Pardo-Manuel de Villena F, Wang W, McMillan L, Threadgill DW. 653  
The polymorphism architecture of mouse genetic resources elucidated using 654  
genome-wide resequencing data: implications for QTL discovery and systems 655  
genetics. *Mamm Genome*. 2007;18: 473–81. doi:10.1007/s00335-007-9045-1 656

22. Durrant C, Tayem H, Yalcin B, Cleak J, Goodstadt L, Villena FP De, et al. 657  
Collaborative Cross mice and their power to map host susceptibility to 658  
*Aspergillus fumigatus* infection Collaborative Cross mice and their power to 659  
map host susceptibility to *Aspergillus fumigatus* infection. 2011; 660  
doi:10.1101/gr.118786.110 661

23. Atamni HJA-T, Mott R, Soller M, Iraqi FA. High-fat-diet induced development 662  
of increased fasting glucose levels and impaired response to intraperitoneal 663  
glucose challenge in the collaborative cross mouse genetic reference 664  
population. *BMC Genet. BioMed Central*; 2016;17: 10. doi:10.1186/s12863- 665  
015-0321-x 666

24. Yalcin B, Flint J, Mott R. Using progenitor strain information to identify 667  
quantitative trait nucleotides in outbred mice. *Genetics*. 2005;171: 673–81. 668  
doi:10.1534/genetics.104.028902 669

25. Kim K, Punj V, Kim J-M, Lee S, Ulmer TS, Lu W, et al. MMP-9 facilitates 670  
selective proteolysis of the histone H3 tail at genes necessary for proficient 671

- osteoclastogenesis. *Genes Dev.* 2016;30: 208–19. doi:10.1101/gad.268714.115 672
26. St. John HC, Bishop KA, Meyer MB, Benkusky NA, Leng N, Kendziorski C, 673  
et al. The Osteoblast to Osteocyte Transition: Epigenetic Changes and 674  
Response to the Vitamin D<sub>3</sub> Hormone. *Mol Endocrinol.* 2014;28: 1150–1165. 675  
doi:10.1210/me.2014-1091 676
27. Broman KW. The genomes of recombinant inbred lines. *Genetics.* 2005;169: 677  
1133–46. doi:10.1534/genetics.104.035212 678
28. Zhang X, Zhang J, Bauer A, Zhang L, Selinger DW, Lu CX, et al. Fine-tuning 679  
BMP7 signalling in adipogenesis by UBE2O/E2-230K-mediated 680  
monoubiquitination of SMAD6. *EMBO J.* 2013;32: 996–1007. 681  
doi:10.1038/emboj.2013.38 682
29. Horiki M, Imamura T, Okamoto M, Hayashi M, Murai J, Myoui A, et al. 683  
Smad6/Smurf1 overexpression in cartilage delays chondrocyte hypertrophy and 684  
causes dwarfism with osteopenia. *J Cell Biol.* 2004;165: 433–45. 685  
doi:10.1083/jcb.200311015 686
30. Estrada KD, Retting KN, Chin AM, Lyons KM. Smad6 is essential to limit 687  
BMP signaling during cartilage development. *J Bone Miner Res.* 2011;26: 688  
2498–510. doi:10.1002/jbmr.443 689
31. Kotkamp K, Mössner R, Allen A, Onichtchouk D, Driever W. A Pou5f1/Oct4 690  
dependent Klf2a, Klf2b, and Klf17 regulatory sub-network contributes to EVL 691  
and ectoderm development during zebrafish embryogenesis. *Dev Biol.* 692  
2014;385: 433–47. doi:10.1016/j.ydbio.2013.10.025 693
32. Wu L, Wary KK, Revskoy S, Gao X, Tsang K, Komarova YA, et al. Histone 694  
Demethylases KDM4A and KDM4C Regulate Differentiation of Embryonic 695



- Stem Cells to Endothelial Cells. *Stem cell reports*. 2015;5: 10–21. 696  
doi:10.1016/j.stemcr.2015.05.016 697
33. Collin-Osdoby P. Role of vascular endothelial cells in bone biology. *J Cell Biochem*. 1994;55: 304–9. doi:10.1002/jcb.240550306 698  
699
34. Kokosar M, Benrick A, Perfilyev A, Fornes R, Nilsson E, Maliqueo M, et al. 700  
Epigenetic and Transcriptional Alterations in Human Adipose Tissue of 701  
Polycystic Ovary Syndrome. *Sci Rep*. 2016;6: 22883. doi:10.1038/srep22883 702
35. Kamei Y, Suganami T, Ehara T, Kanai S, Hayashi K, Yamamoto Y, et al. 703  
Increased expression of DNA methyltransferase 3a in obese adipose tissue: 704  
studies with transgenic mice. *Obesity (Silver Spring)*. 2010;18: 314–21. 705  
doi:10.1038/oby.2009.246 706
36. Miura M, Chen X-D, Allen MR, Bi Y, Gronthos S, Seo B-M, et al. A crucial 707  
role of caspase-3 in osteogenic differentiation of bone marrow stromal stem 708  
cells. *J Clin Invest*. 2004;114: 1704–13. doi:10.1172/JCI20427 709
37. Juraver-Geslin HA, Ausseil JJ, Wassef M, Durand BC. Barhl2 limits growth of 710  
the diencephalic primordium through Caspase3 inhibition of beta-catenin 711  
activation. *Proc Natl Acad Sci U S A*. 2011;108: 2288–93. 712  
doi:10.1073/pnas.1014017108 713
38. Larrain J, Bachiller D, Lu B, Agius E, Piccolo S, De Robertis EM. BMP- 714  
binding modules in chordin: a model for signalling regulation in the 715  
extracellular space. *Development*. 2000;127: 821–30. Available: 716  
[http://www.pubmedcentral.nih.gov/articlerender.fcgi?artid=2280033&tool=pm](http://www.pubmedcentral.nih.gov/articlerender.fcgi?artid=2280033&tool=pmcentrez&rendertype=abstract) 717  
[centrez&rendertype=abstract](http://www.pubmedcentral.nih.gov/articlerender.fcgi?artid=2280033&tool=pmcentrez&rendertype=abstract) 718
39. Davis AM, Mao J, Naz B, Kohl JA, Rosenfeld CS. Comparative effects of 719

- estradiol, methyl-piperidino-pyrazole, raloxifene, and ICI 182 780 on gene 720  
expression in the murine uterus. *J Mol Endocrinol.* 2008;41: 205–17. 721  
doi:10.1677/JME-08-0029 722
40. Kameda T, Mano H, Yuasa T, Mori Y, Miyazawa K, Shiokawa M, et al. 723  
Estrogen inhibits bone resorption by directly inducing apoptosis of the bone- 724  
resorbing osteoclasts. *J Exp Med.* 1997;186: 489–95. Available: 725  
[http://www.pubmedcentral.nih.gov/articlerender.fcgi?artid=2199029&tool=pm](http://www.pubmedcentral.nih.gov/articlerender.fcgi?artid=2199029&tool=pmcentrez&rendertype=abstract) 726  
[centrez&rendertype=abstract](http://www.pubmedcentral.nih.gov/articlerender.fcgi?artid=2199029&tool=pmcentrez&rendertype=abstract) 727
41. Ding Q, Chen H, Xie X, Libby RT, Tian N, Gan L. BARHL2 differentially 728  
regulates the development of retinal amacrine and ganglion neurons. *J* 729  
*Neurosci.* 2009;29: 3992–4003. doi:10.1523/JNEUROSCI.5237-08.2009 730
42. Mo Z, Li S, Yang X, Xiang M. Role of the Barhl2 homeobox gene in the 731  
specification of glycinergic amacrine cells. *Development.* 2004;131: 1607–18. 732  
doi:10.1242/dev.01071 733
43. Shi Y, Li Y, Zhang D, Zhang H, Li Y, Lu F, et al. Exome sequencing identifies 734  
ZNF644 mutations in high myopia. *PLoS Genet.* 2011;7: e1002084. 735  
doi:10.1371/journal.pgen.1002084 736
44. Chen JC, Brown B, Schmid KL. Evaluation of inner retinal function in myopia 737  
using oscillatory potentials of the multifocal electroretinogram. *Vision Res.* 738  
2006;46: 4096–103. doi:10.1016/j.visres.2006.07.033 739
45. Pohlandt F. Hypothesis: myopia of prematurity is caused by postnatal bone 740  
mineral deficiency. *Eur J Pediatr.* 1994;153: 234–6. Available: 741  
<http://www.ncbi.nlm.nih.gov/pubmed/8194552> 742
46. Wang Q, Xue M-L, Zhao G-Q, Liu M-G, Ma Y-N, Ma Y. Form-deprivation 743

- myopia induces decreased expression of bone morphogenetic protein-2, 5 in guinea pig sclera. *Int J Ophthalmol.* 2015;8: 39–45. doi:10.3980/j.issn.2222-3959.2015.01.07
47. Pruitt KD, Brown GR, Hiatt SM, Thibaud-Nissen F, Astashyn A, Ermolaeva O, et al. RefSeq: an update on mammalian reference sequences. *Nucleic Acids Res.* 2014;42: D756-63. doi:10.1093/nar/gkt1114
48. Chang SC, Hoang B, Thomas JT, Vukicevic S, Luyten FP, Ryba NJ, et al. Cartilage-derived morphogenetic proteins. New members of the transforming growth factor-beta superfamily predominantly expressed in long bones during human embryonic development. *J Biol Chem.* 1994;269: 28227–34. Available: <http://www.ncbi.nlm.nih.gov/pubmed/7961761>
49. Settle SH, Rountree RB, Sinha A, Thacker A, Higgins K, Kingsley DM. Multiple joint and skeletal patterning defects caused by single and double mutations in the mouse *Gdf6* and *Gdf5* genes. *Dev Biol.* 2003;254: 116–30. Available: <http://www.ncbi.nlm.nih.gov/pubmed/12606286>
50. Verga Falzacappa MV, Casanovas G, Hentze MW, Muckenthaler MU. A bone morphogenetic protein (BMP)-responsive element in the hepcidin promoter controls HFE2-mediated hepatic hepcidin expression and its response to IL-6 in cultured cells. *J Mol Med (Berl).* 2008;86: 531–40. doi:10.1007/s00109-008-0313-7
51. Angelopoulos NG, Goula AK, Papanikolaou G, Tolis G. Osteoporosis in HFE2 juvenile hemochromatosis. A case report and review of the literature. *Osteoporos Int.* 2006;17: 150–5. doi:10.1007/s00198-005-1920-6
52. Baron R, Kneissel M. WNT signaling in bone homeostasis and disease: from

human mutations to treatments. *Nat Med.* Nature Publishing Group, a division of Macmillan Publishers Limited. All Rights Reserved.; 2013;19: 179–92. doi:10.1038/nm.3074

53. Brack AS, Murphy-Seiler F, Hanifi J, Deka J, Eyckerman S, Keller C, et al. BCL9 is an essential component of canonical Wnt signaling that mediates the differentiation of myogenic progenitors during muscle regeneration. *Dev Biol.* 2009;335: 93–105. doi:10.1016/j.ydbio.2009.08.014

54. Karasik D, Kiel DP. Genetics of the musculoskeletal system: a pleiotropic approach. *J Bone Miner Res.* 2008;23: 788–802. doi:10.1359/jbmr.080218

55. Bai S, Kopan R, Zou W, Hilton MJ, Ong C, Long F, et al. NOTCH1 regulates osteoclastogenesis directly in osteoclast precursors and indirectly via osteoblast lineage cells. *J Biol Chem.* 2008;283: 6509–18. doi:10.1074/jbc.M707000200

56. Regan J, Long F. Notch signaling and bone remodeling. *Curr Osteoporos Rep.* 2013;11: 126–9. doi:10.1007/s11914-013-0145-4

57. Canalis E, Zanotti S. Hajdu-Cheney syndrome: a review. *Orphanet J Rare Dis.* BioMed Central; 2014;9: 200. doi:10.1186/s13023-014-0200-y

58. Jeyabalan J, Shah M, Viollet B, Chenu C. AMP-activated protein kinase pathway and bone metabolism. *J Endocrinol.* 2012;212: 277–90. doi:10.1530/JOE-11-0306

59. Lemberg MK, Freeman M. Functional and evolutionary implications of enhanced genomic analysis of rhomboid intramembrane proteases. *Genome Res.* 2007;17: 1634–1646. doi:10.1101/gr.6425307

60. Adrain C, Zettl M, Christova Y, Taylor N, Freeman M, References A. Supporting Online Material for. 2012;225. doi:10.1126/science.1214400

61.	McIlwain DR, Lang PA, Maretzky T, Hamada K, Ohishi K, Maney SK, et al.	792
	iRhom2 Regulation of TACE Controls TNF-Mediated Protection Against	793
	Listeria and Responses to LPS. <i>Science</i> (80- ). 2012;335: 229–232.	794
	doi:10.1126/science.1214448	795
62.	Siggs OM, Grieve A, Xu H, Bambrough P, Christova Y, Freeman M. Genetic	796
	interaction implicates iRhom2 in the regulation of EGF receptor signalling in	797
	mice. <i>Biol Open</i> . 2014;3.	798
63.	Hosur V, Johnson KR, Burzenski LM, Stearns TM, Maser RS, Shultz LD.	799
	Rhbdf2 mutations increase its protein stability and drive EGFR hyperactivation	800
	through enhanced secretion of amphiregulin. <i>Proc Natl Acad Sci</i> . 2014;111:	801
	E2200–E2209. doi:10.1073/pnas.1323908111	802
64.	Li X, Maretzky T, Weskamp G, Monette S, Qing X, Issuree PDA, et al.	803
	iRhoms 1 and 2 are essential upstream regulators of ADAM17-dependent	804
	EGFR signaling. <i>Proc Natl Acad Sci U S A. National Academy of Sciences</i> ;	805
	2015;112: 6080–5. doi:10.1073/pnas.1505649112	806
65.	Luo W-W, Li S, Li C, Lian H, Yang Q, Zhong B, et al. iRhom2 is essential for	807
	innate immunity to DNA viruses by mediating trafficking and stability of the	808
	adaptor STING. <i>Nat Immunol</i> . 2016;17: 1057–1066. doi:10.1038/ni.3510	809
66.	Siggs OM, Xiao N, Wang Y, Shi H, Tomisato W, Li X, et al. iRhom2 is	810
	required for the secretion of mouse TNF $\alpha$ . <i>Blood. American Society of</i>	811
	<i>Hematology</i> ; 2012;119: 5769–71. doi:10.1182/blood-2012-03-417949	812
67.	Adrain C, Zettl M, Christova Y, Taylor N, Freeman M. Tumor Necrosis Factor	813
	Signaling Requires iRhom2 to Promote Trafficking and Activation of TACE.	814
	<i>Science</i> (80- ). 2012;335: 225–228. doi:10.1126/science.1214400	815

68. Udagawa N, Takahashi N, Akatsu T, Tanaka H, Sasaki T, Nishihara T, et al. 816  
Origin of osteoclasts: mature monocytes and macrophages are capable of 817  
differentiating into osteoclasts under a suitable microenvironment prepared by 818  
bone marrow-derived stromal cells. Proc Natl Acad Sci U S A. National 819  
Academy of Sciences; 1990;87: 7260–4. Available: 820  
<http://www.ncbi.nlm.nih.gov/pubmed/2169622> 821
69. Issuree PDA, Maretzky T, McIlwain DR, Monette S, Qing X, Lang PA, et al. 822  
iRHOM2 is a critical pathogenic mediator of inflammatory arthritis. J Clin 823  
Invest. American Society for Clinical Investigation; 2013;123: 928–32. 824  
doi:10.1172/JCI66168 825
70. Qing X, D. Rogers L, Mortha A, Lavin Y, Redecha P, Issuree PD, et al. 826  
iRhom2 regulates CSF1R cell surface expression and non-steady state 827  
myelopoiesis in mice. Eur J Immunol. 2016;46: 2737–2748. 828  
doi:10.1002/eji.201646482 829
71. Blaydon DC, Etheridge SL, Risk JM, Hennies H-C, Gay LJ, Carroll R, et al. 830  
RHBDF2 mutations are associated with tylosis, a familial esophageal cancer 831  
syndrome. Am J Hum Genet. Elsevier; 2012;90: 340–6. 832  
doi:10.1016/j.ajhg.2011.12.008 833
72. Kobayashi K, Takahashi N, Jimi E, Udagawa N, Takami M, Kotake S, et al. 834  
Tumor necrosis factor alpha stimulates osteoclast differentiation by a 835  
mechanism independent of the ODF/RANKL-RANK interaction. J Exp Med. 836  
2000;191: 275–86. Available: 837  
[http://www.pubmedcentral.nih.gov/articlerender.fcgi?artid=2195746&tool=pm 838](http://www.pubmedcentral.nih.gov/articlerender.fcgi?artid=2195746&tool=pmcentrez&rendertype=abstract)  
centrez&rendertype=abstract 839

73. Yi T, Lee H-L, Cha J-H, Ko S-I, Kim H-J, Shin H-I, et al. Epidermal growth factor receptor regulates osteoclast differentiation and survival through cross-talking with RANK signaling. *J Cell Physiol.* 2008;217: 409–422. doi:10.1002/jcp.21511
74. Hosur V, Johnson KR, Burzenski LM, Stearns TM, Maser RS, Shultz LD. *Rhbdf2* mutations increase its protein stability and drive EGFR hyperactivation through enhanced secretion of amphiregulin. *Proc Natl Acad Sci.* 2014;111: E2200–E2209. doi:10.1073/pnas.1323908111
75. Hung JY, Horn D, Woodruff K, Prihoda T, LeSaux C, Peters J, et al. Colony-stimulating factor 1 potentiates lung cancer bone metastasis. *Lab Invest.* 2014;94: 371–381. doi:10.1038/labinvest.2014.1
76. Qing X, D. Rogers L, Mortha A, Lavin Y, Redecha P, Issuree PD, et al. *iRhom2* regulates CSF1R cell surface expression and non-steady state myelopoiesis in mice. *Eur J Immunol.* 2016;46: 2737–2748. doi:10.1002/eji.201646482
77. Hiram-Bab S, Liron T, Deshet-Unger N, Mittelman M, Gassmann M, Rauner M, et al. Erythropoietin directly stimulates osteoclast precursors and induces bone loss. *FASEB J.* 2015;29: 1890–900. doi:10.1096/fj.14-259085
78. Rügsegger P, Koller B, Müller R. A microtomographic system for the nondestructive evaluation of bone architecture. *Calcif Tissue Int.* 1996;58: 24–29. doi:10.1007/BF02509542
79. Hildebrand T, Laib A, Müller R, Dequeker J, Rügsegger P. Direct three-dimensional morphometric analysis of human cancellous bone: microstructural data from spine, femur, iliac crest, and calcaneus. *J Bone Miner Res.* 1999;14:

	1167–74. doi:10.1359/jbmr.1999.14.7.1167	864
80.	Bouxsein ML, Boyd SK, Christiansen BA, Guldberg RE, Jepsen KJ, Müller R. Guidelines for assessment of bone microstructure in rodents using micro-computed tomography. J Bone Miner Res. 2010;25: 1468–86. doi:10.1002/jbmr.141	865 866 867 868
81.	Hall M, Manship G, Morahan G, Pettit K, Scholten J, Tweedie K, et al. The genome architecture of the Collaborative Cross mouse genetic reference population. Genetics. 2012;190: 389–401. doi:10.1534/genetics.111.132639	869 870 871
82.	Mott R, Talbot CJ, Turri MG, Collins a C, Flint J. A method for fine mapping quantitative trait loci in outbred animal stocks. Proc Natl Acad Sci U S A. 2000;97: 12649–54. doi:10.1073/pnas.230304397	872 873 874
83.	Hochberg Y. Controlling the False Discovery Rate : A Practical and Powerful Approach to Multiple Testing Author ( s ): Yoav Benjamini and Yosef Hochberg Source : Journal of the Royal Statistical Society . Series B ( Methodological ), Vol . 57 , No . 1 ( 1995 ), Publi. 2016;57: 289–300.	875 876 877 878
84.	Li H. A quick method to calculate QTL confidence interval. J Genet. 2011;90: 355–60. Available: <a href="http://www.ncbi.nlm.nih.gov/pubmed/21869489">http://www.ncbi.nlm.nih.gov/pubmed/21869489</a>	879 880
85.	Trapnell C, Pachter L, Salzberg SL. TopHat: discovering splice junctions with RNA-Seq. Bioinformatics. Oxford University Press; 2009;25: 1105–11. doi:10.1093/bioinformatics/btp120	881 882 883
	<b>Figure legends</b>	884
	<b>Figure 1.</b> $\mu$ CT images of trabecular and cortical bone of the femora of representative male CC mice. <b>(A)</b> Trabecular bone. Left: IL-2452, Right: IL-1513. <b>(B)</b> Cortical bone. Left: IL-785, Right: IL-2689.	885 886 887



**Figure 2** Trabecular and cortical traits distributions across the CC lines. X-axis is the lines, y-axis is the trait means **A**. From top left, counter-clockwise: BV/TV (%), Tb.N (mm<sup>-1</sup>), Tb.Th (um), Conn.D (mm<sup>-3</sup>), SMI, and Tb.Sp (mm). **B**. Left, vBMD (mgHA/cm<sup>3</sup>), right, Ct.Th (mm). Color codes group line(s) which significantly differ from other groups. Lines are ordered inconsistently among the traits, per trait-specific descending order. Refer to Table S3 for more details.

**Figure 3** Haplotype association maps for the trabecular and cortical traits. X-axis is the position on the chromosome, y-axis is the  $-\log P$  value of the association. Lower threshold represents the 95<sup>th</sup> percentile of 200 simulations, and top represents the 99<sup>th</sup> percentile. Loci above the 99% cut-off were further investigated. From top to bottom: BV/TV, Tb.N, Tb.Th, Tb.Sp, vBMD, and Ct.Th.

**Figure 4.** Ancestral effects relative to WSB. Y axis is the strain deviation relative to WSB, x axis is the different strains of the eight CC founders. **(A)** to **(F)**: *Trl7* to *Trl9*, *Crll*, and *Crl2*, respectively.

**Figure 5** Traits distribution at the marker UNC20471277 across bearers of homozygous and heterozygous alleles, separated by sex. X-axis is the allelic variation at the marker, y-axis is the trait value.

**Figure 6** Merge analysis. Readings below  $\log P = 4$  are elided for brevity. X axis is the position on the genome in Mb; y left axis is the  $\log P$  score; y right axis is the recombination rate scale; colored bars are genes (note that only strong putative candidate genes are shown.); cyan line is the recombination rate; black continues line is the haplotype test's peak; dashed line is the 99% permutation threshold. **(A)** to **(F)**: Trl7 of BV/TV, Trl7 of Tb.N, Trl8 of Tb.Th, Trl9 of Tb.Sp, Crl1 of Ct.Th, and Crl2 of vBMD, respectively.

**Figure 7** *Rhbd2* knockout versus wildtype for each of the studied traits. Left is KO, right is WT. PV is the confounder-adjusted P value. The unadjusted P value is in brackets. PV = 0 means PV < 0.001.

**Figure 8**  $\mu$ CT images of three-dimensional representative cortical and trabecular bones reconstructions for *Rhbd2* knockout and wildtype. Left: KO, right: WT. **(A)** Trabecular bone. **(B)** Cortical bone. All samples were of male mice, aged 11 weeks.

Supporting information captions

**Figure S1** *Trait distributions for Males and Females*. **A1, A2**: Trabecular and cortical bone, respectively, males. **B1, B2**: trabecular and cortical bone, respectively, females. X-axis is the lines, y-axis is the trait means **A**. From top left, counter-clockwise: BV/TV (%), Tb.N (mm<sup>-1</sup>), Tb.Th (um), Conn.D (mm<sup>-3</sup>), SMI, and Tb.Sp (mm). **B**: Left, vBMD (mgHA/cm<sup>3</sup>); right, Ct.Th (mm). Color codes group line(s) which

significantly differ from other groups. Lines are ordered inconsistently among the 930  
traits, according to trait-specific descending order. 931

932

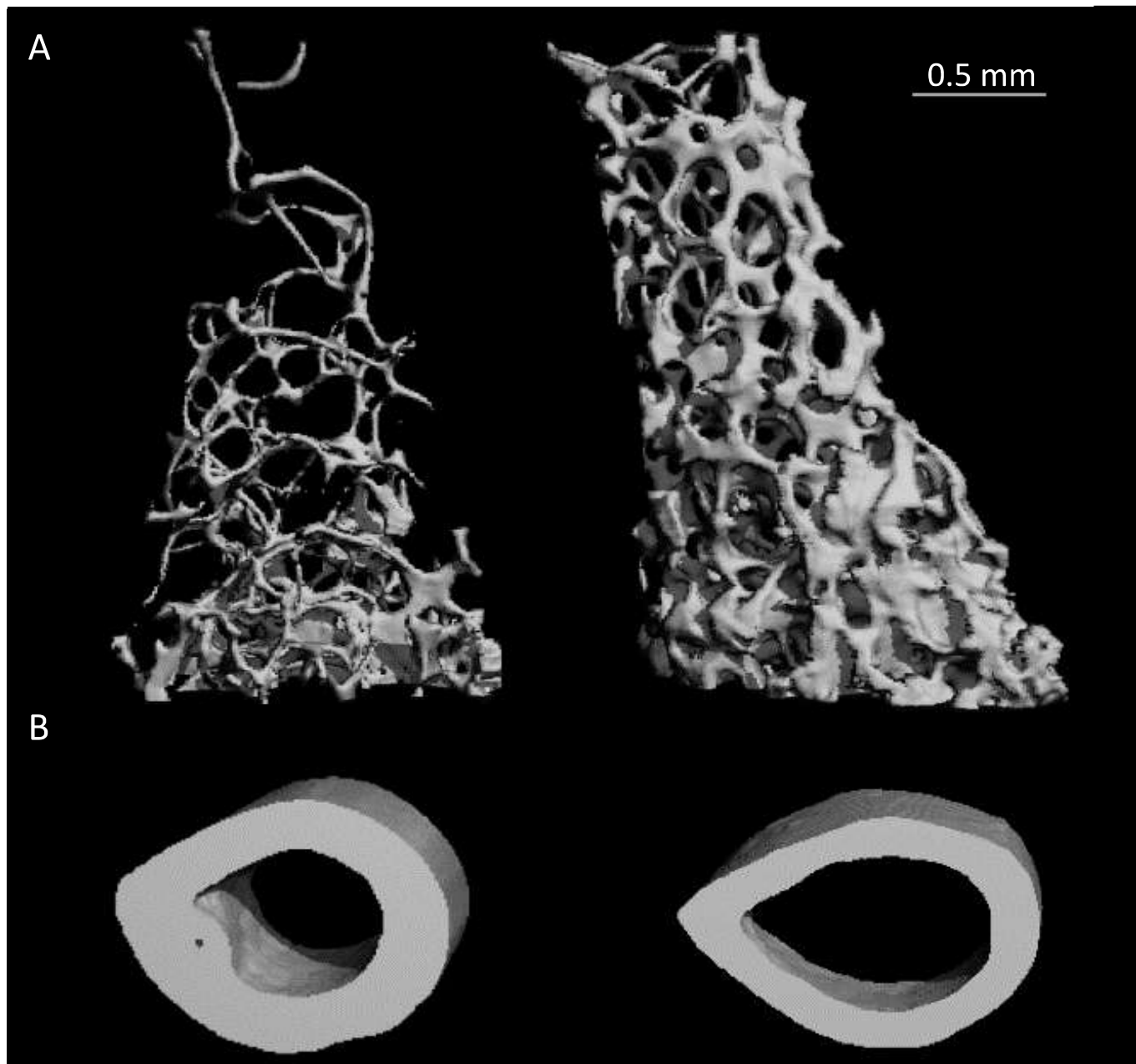
**Figure S2** *Haplotype association maps for the trabecular and cortical traits.* X-axis 933  
is the position on the chromosome, y-axis is the  $-\log P$  value of the association. Lower 934  
threshold represents the 95th percentile of 200 simulations, and top represents the 9th 935  
percentile. Loci above the 99% cut-off were further investigated. From top to bottom: 936  
Conn.D, SMI. 937

**Figure S3** *Confidence interval simulations.* Loci at a neighborhood of 3-5 Mb around 938  
the original locus were simulated by permuting the residual sum of squares of the 939  
related phenotype. Maximum logP was obtained along with its relative position in Mb 940  
to the original QTL (histograms, left panels), and with the number of markers from 941  
the original QTL (boxplots, right panels). (A) and (B) show simulations results for the 942  
BV/TV and Tb.N loci. These determined with high confidence that the peak QTL is 943  
responsible for the effect seen in the haplotype scan, thus the narrow CI; (C) to (F) 944  
show simulation results for Tb.Th, Tb.Sp, Ct.Th, and vBMD, 945  
respectively; note the narrow CI for *Crl2* (vBMD), wide for *Trl8* (Tb.Th), and wider 946  
still for *Crll*(Ct.Th). 947

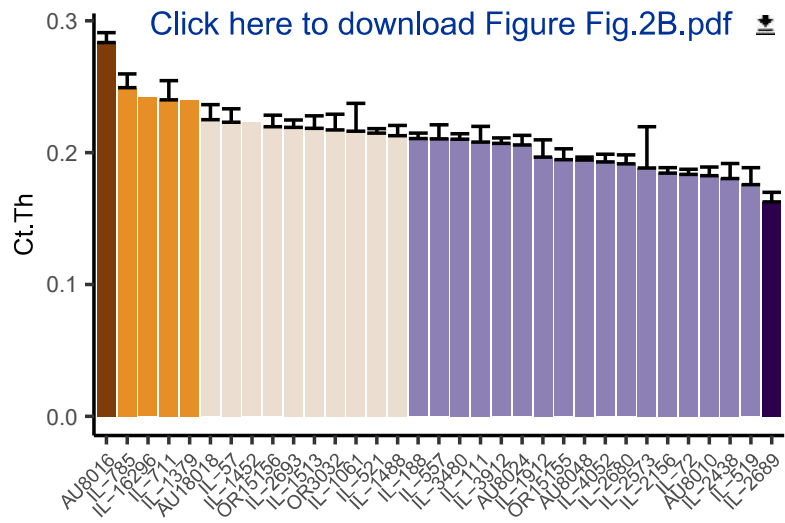
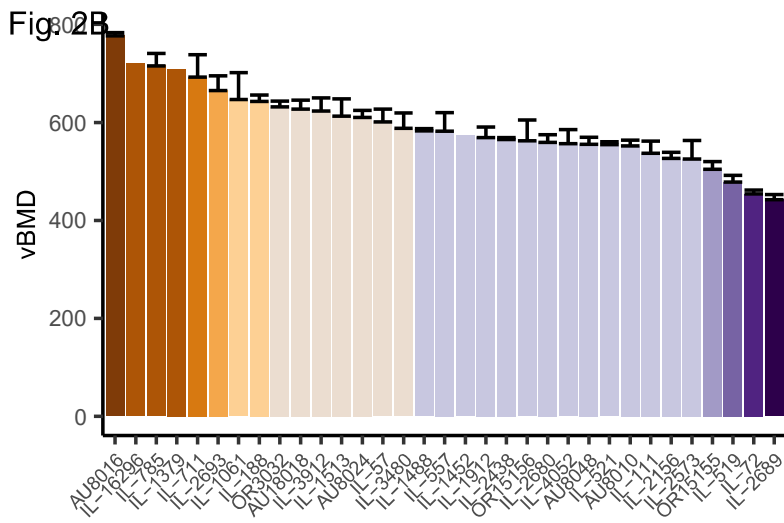
**Figure S4** *RNA-seq of osteoclasts.* Gene names are on the right of each plot. Green 948  
represents plus-stranded genes, black represents minus-stranded genes. Y-axis is the 949  
raw expression count, where the negative scale refers to minus-stranded gene count. 950  
Each bracket corresponds to a particular gene; left-to-right green (black) brackets fit 951  
green (black) top-to-bottom gene-names. 952

<b>Figure S5</b> <i>RNA-seq of osteocytes</i> . Gene names are on the right of each plot. Orange	953
represents plus-stranded genes, black represents minus-stranded genes. Y-axis is the	954
raw expression count, where the negative scale refers to minus-stranded gene count.	955
Each bracket corresponds to a particular gene; left-to-right orange (black) brackets fit	956
orange (black) top-to-bottom gene names	957
<b>Table S1</b> <i>Pearson's correlations between measured <math>\mu</math>CT traits</i> . Pairwise correlations	958
for each trait are given as Pearson's <i>r</i> . In bold are the 5 most strong correlations.	959
<b>Table S2</b> <i>Covariates effects</i> . <i>LogP</i> is the negative logarithm of <i>P</i> value. Effects of	960
covariates (i.e., the degree to which each covariate explains the phenotypic	961
difference). Values were determined by regressing the covariates along with the CC	962
lines, and running an ANOVA test. Note the covariates prominent effect on the	963
cortical traits. The batch effect was the strongest, affecting Tb.Th, Ct.Th, and vBMD.	964
	965
<b>Table S3</b> <i>Trait values per CC line included in this study (for both sexes combined)</i> .	966
Trait means for each line, including number of members and standard error (SE). NA	967
means data were not available.	968
	969
<b>Table S4</b> <i>A comprehensive list of all genes under the 95% confidence-interval (CI)</i>	970
<i>for the QTLs identified in this study</i> . Light blue is the 95% CI region; blue is the 90%	971
CI region; and pink is the 50% CI region. Merge strength column gives the	972
normalized dosage of merge logP values as outlined in the methods section. Gene	973
symbols in bold type are discussed in the manuscript. Genes under the QTLs for the	974
cortical and trabecular traits. Light blue is the 95% CI, blue is the 90% CI, and red is	975
the 50% CI. "Merge Strength" refers to the proportion of merge logP values	976

constricted to the region of the specific gene. Note that for *Trl7* which is common to 977  
BV/TV and Tb.N, the average values between the two are provided. 978









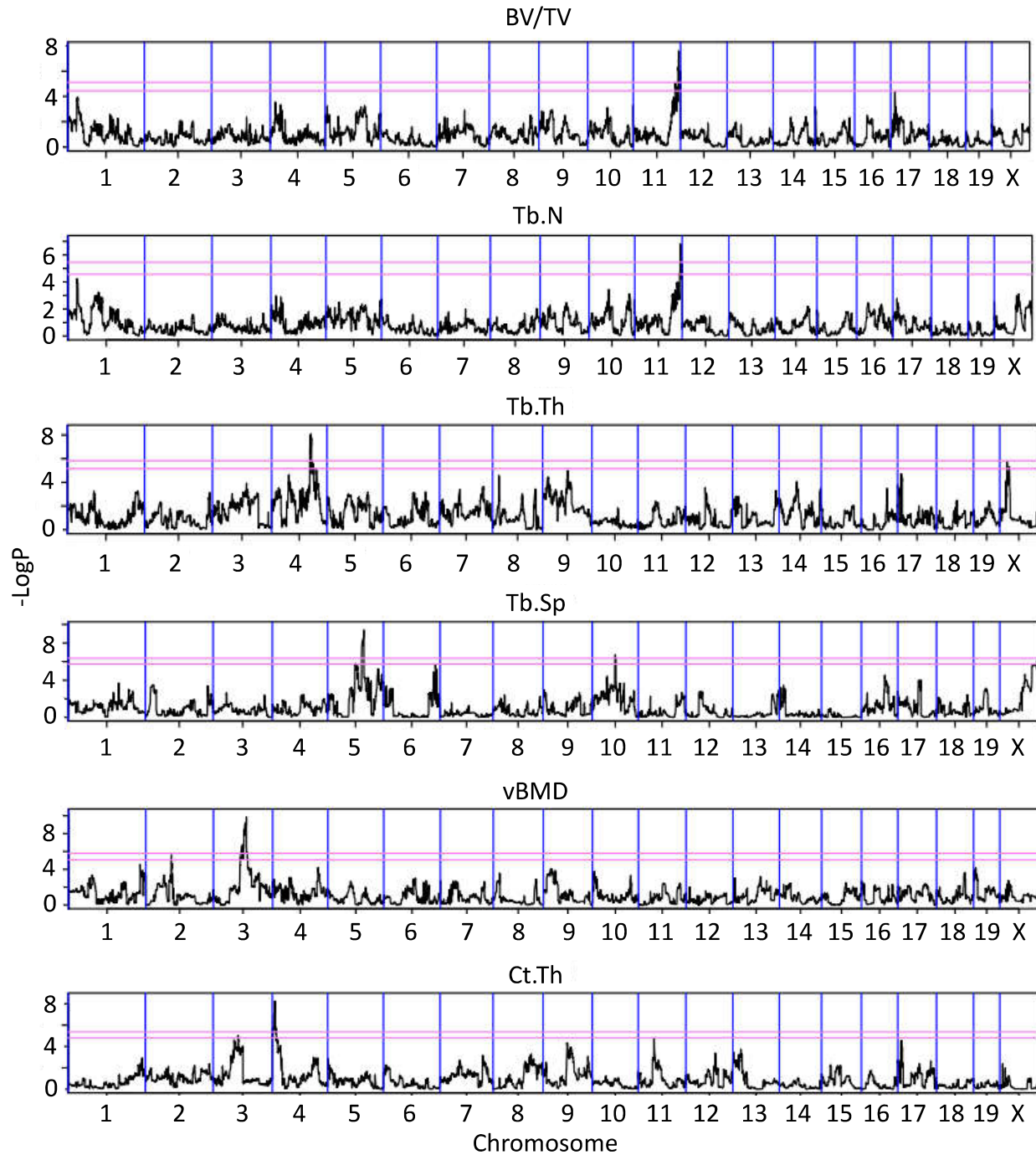


Fig. 4

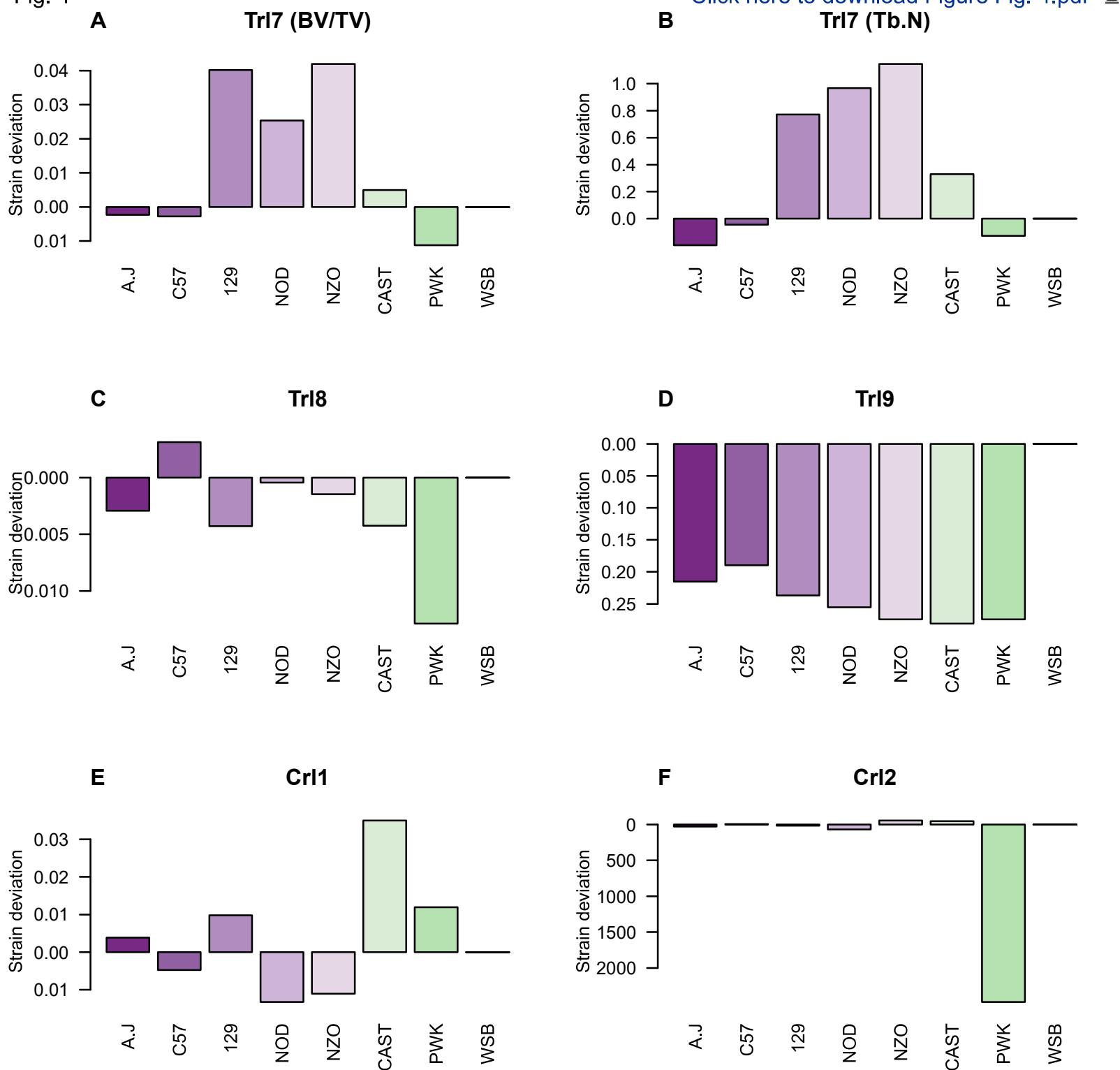


Fig. 5

[Click here to download Figure Fig.5.pdf](#) 

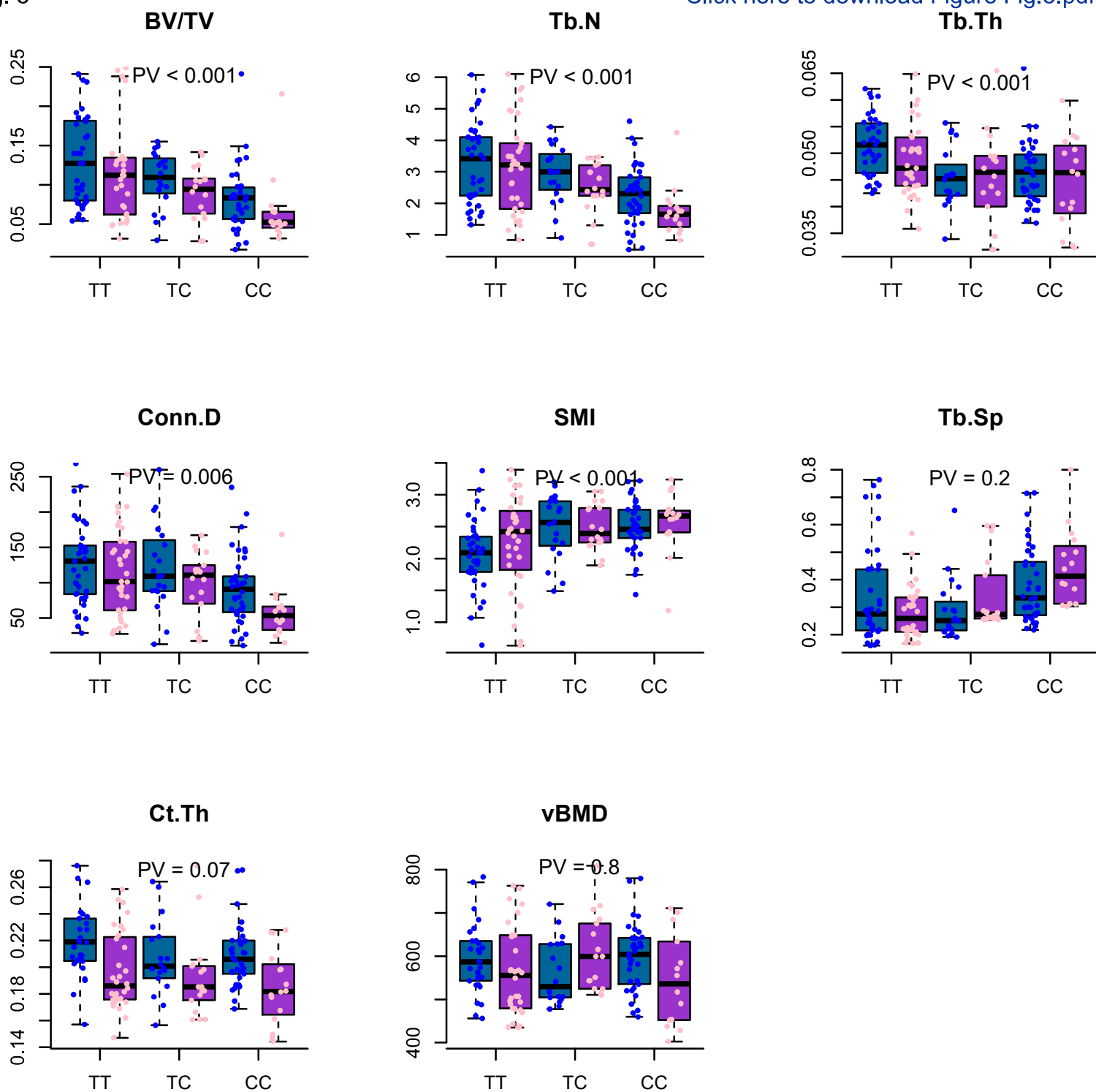


Fig. 6

[Click here to download Figure Fig.6.pdf](#)

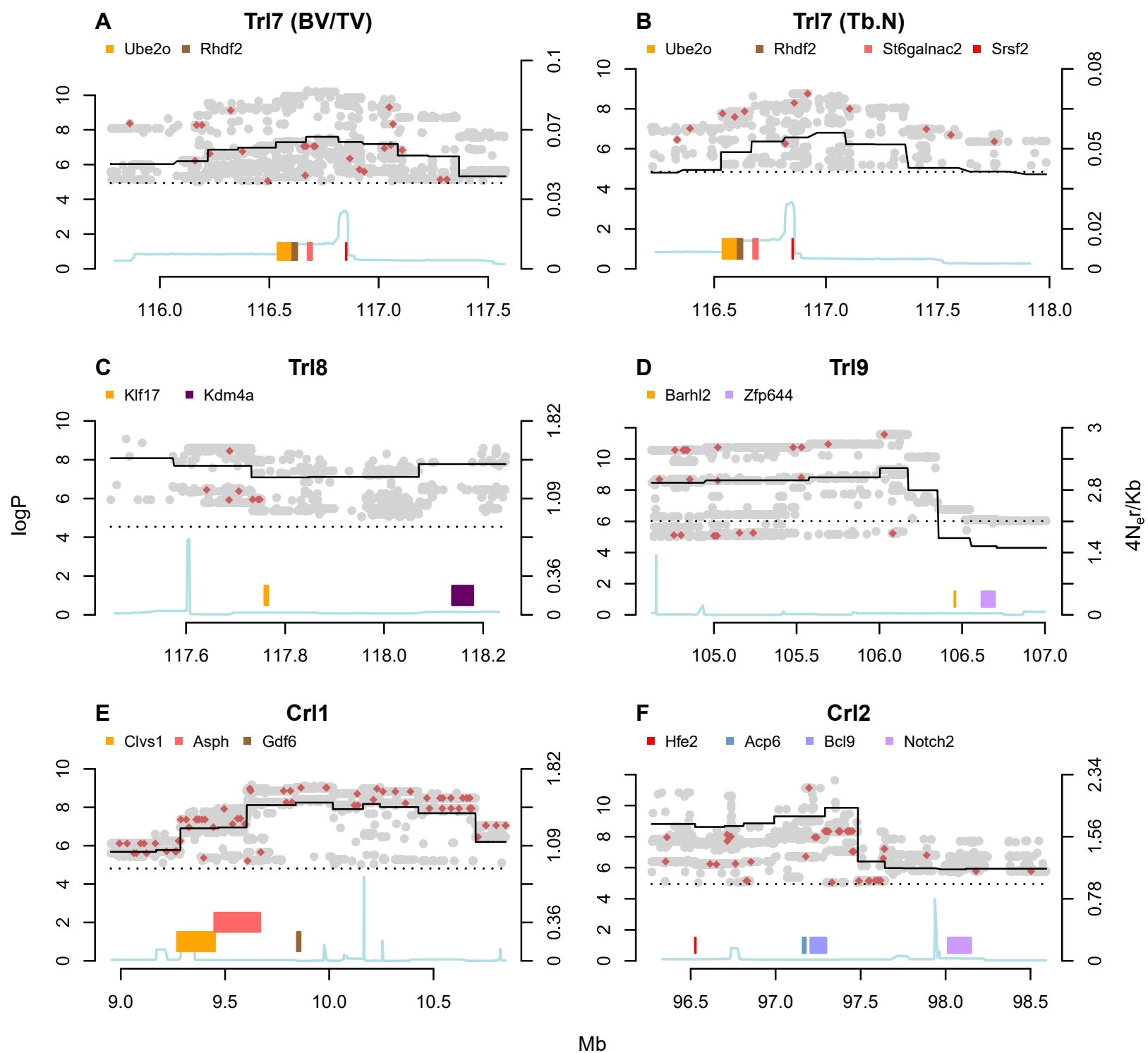


Fig. 7

[Click here to download Figure Fig.7.pdf](#) 

